



Pulsating heat pipes: basics of functioning and modeling

Vadim Nikolayev, Marco Marengo

► To cite this version:

Vadim Nikolayev, Marco Marengo. Pulsating heat pipes: basics of functioning and modeling. John R. Thome. Encyclopedia of Two-Phase Heat Transfer and Flow IV, , pp.63-139, 2018, 9789813234369. 10.1142/9789813234406_0002 . cea-03261340

HAL Id: cea-03261340

<https://hal-cea.archives-ouvertes.fr/cea-03261340>

Submitted on 15 Jun 2021

HAL is a multi-disciplinary open access archive for the deposit and dissemination of scientific research documents, whether they are published or not. The documents may come from teaching and research institutions in France or abroad, or from public or private research centers.

L'archive ouverte pluridisciplinaire **HAL**, est destinée au dépôt et à la diffusion de documents scientifiques de niveau recherche, publiés ou non, émanant des établissements d'enseignement et de recherche français ou étrangers, des laboratoires publics ou privés.

Chapter 2

Pulsating heat pipes: basics of functioning and modeling

Vadim S. Nikolayev¹ and Marco Marengo²

¹*Service de Physique de l'Etat Condensé, CEA, CNRS, Université Paris-Saclay,
CEA Saclay, 91191 Gif-sur-Yvette Cedex, France,
vadim.nikolayev@cea.fr*

²*School of Computing, Engineering and Mathematics, University of Brighton,
Lewes Road, BN2 4GJ, Brighton, UK*

For cooling of electronic or electric equipment, there is a growing industrial demand of high performance thermal links. One of such thermal devices is the recently invented pulsating (called also oscillating) heat pipe (PHP). It consists in a closed capillary tube folded into meander and partially filled with a liquid. One side of the meander is in thermal contact with a hot spot, the other with a cold spot. The oscillation of the liquid plugs and vapor bubbles spontaneously occurs after the start of heating by the action of evaporation/condensation at the menisci. The plugs move between hot and cold areas by creating an efficient convective heat exchange. This advantage and also the PHP simplicity make it highly competitive with respect to other kinds of heat pipes. However, the PHP functioning is non-stationary and depends on a large number of physical and material parameters. As a result, application of empirical correlations is quite unsuccessful and more sophisticated theoretical and basic experimental studies are necessary. In this chapter we present the current level of understanding and existing approaches to the PHP modeling and design. We start by describing the basic experiments with the simplest, single branch PHP that contains only one bubble-plug couple. We show how the results of these experiments help to understand the PHP functioning and introduce the Reader to the theoretical and numerical approaches to the PHP modeling by describing the relevant physical phenomena. Finally, we review the state of the art of modeling of the multi-branch PHP. This chapter is complementary to the review of the experimental work on multi-branch PHPs presented in Chapter 1.

Contents

| | |
|---------------------------------------------------------------------------------------------------------------------|----|
| 2. Pulsating heat pipes: functioning and modeling | 1 |
| <i>V. S. Nikolayev, M. Marengo</i> | |
| 1. Introduction | 3 |
| 2. Single branch PHP experiments | 5 |
| 2.1. Transparent single branch PHP | 5 |
| 2.2. Assessment of the vapor thermodynamic state | 6 |
| 2.3. Liquid film dynamics in evaporator | 8 |
| 3. Modeling of physical phenomena in the PHP “unit cell” | 10 |
| 3.1. Fluid flow and heat exchange in the liquid domain | 10 |
| 3.1.1. Isothermal Taylor bubbles | 12 |
| 3.1.2. Pressure losses in the liquid phase | 13 |
| 3.1.3. Taylor bubbles under pulsations and heat transfer | 16 |
| 3.2. Physics and modeling of vapor phase | 17 |
| 3.2.1. Vapor thermodynamic state | 18 |
| 3.2.2. Vapor energy equation | 20 |
| 3.3. Liquid films in PHP | 21 |
| 3.3.1. Liquid film deposition by receding meniscus | 22 |
| 3.3.2. Meniscus motion over the preexisting film | 22 |
| 3.3.3. Liquid films at phase change | 24 |
| 3.3.4. Contact line dynamics in the absence of the phase change | 25 |
| 3.3.5. Contact line at evaporation or condensation | 29 |
| 4. Start-up and functioning of the single branch PHP | 34 |
| 4.1. Superheated vapor model | 35 |
| 4.2. Film evaporation-condensation (FEC) model | 38 |
| 4.2.1. FEC model for imposed temperatures in evaporator and condenser | 39 |
| 4.2.2. Introduction of the thermal fluid-solid coupling | 40 |
| 4.3. Liquid heat transfer | 42 |
| 4.4. FEC model: steady regime of single branch PHP | 43 |
| 4.5. Start-up of oscillations in single branch PHP with imposed temperatures in evaporator and condenser: FEC model | 44 |
| 4.6. Start-up of oscillations in single branch PHP with smooth temperature distribution: FEC model | 46 |
| 4.7. Single branch PHP description: beyond FEC model | 49 |
| 5. Two-branch PHP | 50 |
| 5.1. Heat transfer via PHP | 52 |
| 6. Genesis of multi-branch simulation modeling | 53 |
| 6.1. Superheated vapor modeling | 53 |
| 6.2. FEC model: imposed temperatures | 56 |
| 6.3. Bubble generation model by Senjaya and Inoue | 57 |
| 6.4. Simulation of d’Entremont and Thome | 58 |
| 6.5. FEC model with tube heat conduction | 59 |
| 7. 2D and 3D simulations of multi-branch PHP | 65 |
| 8. Conclusions | 66 |
| 9. Acknowledgements | 66 |
| <i>Nomenclature</i> | 68 |
| <i>References</i> | 71 |

1. Introduction

One of the contemporary technological challenges is a reduction of mass of transportation means in order to reduce their energy consumption and CO₂ emission. This requires replacing of metals by lighter synthetic materials (composites, ceramics, etc.), which, however, are poor heat conductors and thus require special thermal management solutions for their cooling capability to handle high heat loads. On the other hand, with the increase of power levels related to the miniaturization of electronics progressing towards multi chip modules, conventional cooling technologies and thermal management are facing growing challenges including the cooling heat fluxes of several hundreds of W/cm², long term reliability, and very low costs for consumer market products, among others. This necessitates the development and use of more efficient, non-traditional cooling approaches. Special devices called heat pipes are used more and more widely to transfer the excessive heat to a colder environment.

A heat pipe is basically a closed container tube filled with the working fluid. One side of this tube (called evaporator) is brought in thermal contact with a hot point to be cooled. The other end (called condenser) is connected to the cold point where the heat can be dissipated. A portion of tube between evaporator and condenser is called adiabatic section. The working fluid and the heat pipe regime are both chosen in such a way that the saturation temperature is between the evaporator temperature T_e and condenser temperature T_c . The liquid is thus vaporized in the evaporator section. The generated vapor is transported due to its expansion to the condenser section and condenses there. The liquid is transported back to the evaporator section and the cycle starts over again. The heat is transferred mainly due to the latent heat absorption in the evaporator and its release in the condenser. Since the latent heat is generally large, the heat pipes are quite efficient. There are different kinds of heat pipes. They differ by their geometry, internal tube structure, and a mechanism of liquid transport from condenser to evaporator.

Pulsating heat pipe (PHP, called sometimes oscillating heat pipe), invented in the early 1990s [Akachi (1993)] present promising alternatives for the conventional heat pipes in situations where removal of high heat fluxes is required. PHP is a capillary tube (with no wick structure) bent into many turns and partially filled with a working fluid (Fig. 1). When the tube is thin enough, liquid plugs and vapor bubbles are formed inside it. When the temperature difference between evaporator and condenser exceeds a certain threshold, the gas bubbles and liquid plugs begin to oscillate spontaneously back and forth. The amplitude of oscillations is quite strong and the liquid plugs penetrate into both condenser and evaporator. The heat is thus transferred not only by the latent heat transfer like in other types of heat pipes, but also by sweeping the hot walls by the colder liquid and vice versa. This phenomenon is the reason of high efficiency of PHPs in comparison with other types of heat pipes. Compared to other cooling solutions, PHPs are simple and thus more reliable and

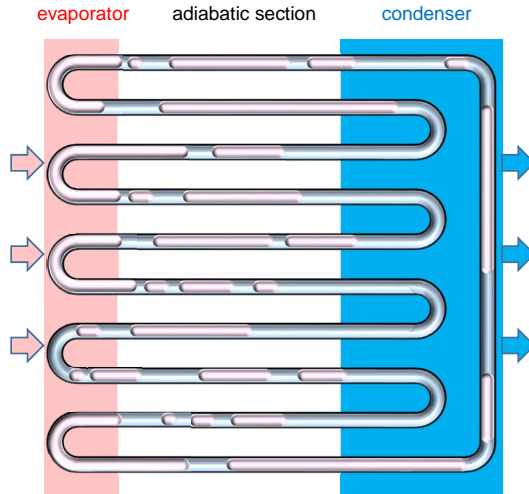


Fig. 1. Schematic representation of the pulsating heat pipe (PHP). The heated (evaporator) sections of the tube are those inside the rose rectangle, while the cooled sections (condenser) are inside the blue rectangle. The tube sections in between are adiabatic. The vapor bubbles and liquid plugs are schematized inside the PHP tube.

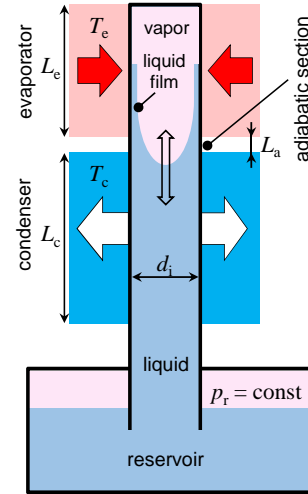


Fig. 2. Detailed scheme of the simplest, single branch PHP.

cheap. However their functioning is not completely understood. A complicated interplay of different hydrodynamic and phase-exchange phenomena needs to be accounted for in the modeling approaches [Khandekar *et al.* (2010); Nikolayev and Sundararaj (2014)]. Unlike other heat transfer devices, the functioning of PHPs is non-stationary and thus difficult to model. Basically, what we know about the PHP design for certain is that the tube diameter should be smaller than the capillary length to avoid liquid-vapor stratification inside the tube. For all the above reasons, PHP is an active field of research, with dozens of publications each year in leading scientific journals.

Historically, there were many attempts to correlate the transferred by PHP heat flux with its other parameters [Zhang and Faghri (2008)]. The predictive capability of these correlations was however unsatisfactory, probably because of non-stationary functioning of PHP. Most importantly, these correlations are unable to predict the very fact of PHP start-up. Direct PHP simulation remains thus an only reliable mean to dimension these devices for industrial needs.

In this chapter, we will review the basic physical phenomena important for the PHP functioning and some experiments with PHPs of the simplest geometries. Then we will apply this knowledge to the PHP modeling and review the state of the art PHP models. This chapter is complementary to the review of the experimental work on multi-branch PHPs presented in Chapter 1.

First of all, a few terminologies need to be fixed. By “evaporator section” we mean a portion of the tube (= a tube section) inside evaporator; they can be many for a PHP. When one follows the PHP tube one goes through evaporator, adiabatic, condenser, adiabatic, evaporator sections, and so on. By “turn” we mean a bent at 180° portion of the tube which is usually belongs to evaporator or condenser sections. Number of PHP turns is the number of its turns *either* in evaporator *or* condenser, i.e. a *half* of total number of turns. By “branch” we mean a tube section linking the centers of evaporator and condenser sections. The total number of branches is twice the number of turns. For instance, the 5-turn PHP represented in Fig. 1 has 10 branches. The feedback section is that connecting the first and last PHP branches. It is vertical in Fig. 28. It may be nonexistent if PHP is folded in the 3rd dimension. By “plug” we mean the liquid domain inside the tube and by “bubble”, the vapor domain.

2. Single branch PHP experiments

The discussion of PHP is reasonable to start with its simplest version, the single branch PHP (Fig. 2). It is a straight capillary with a sealed end, which is heated (evaporator). The middle part of the capillary is cooled and is thus condenser. A single gas bubble is confined between the sealed end and a liquid plug. The condenser end of the capillary is connected to a large reservoir maintained at a constant pressure p_r . Once the necessary value of temperature difference between evaporator and condenser is established, the liquid meniscus starts oscillating in the vertical direction. One can see that such a system represents a kind of a “unit cell” for the more complex multi-branch PHP of Fig. 1 and thus is important to understand.

2.1. Transparent single branch PHP

Extensive information about the PHP-related phenomena has been obtained in the PHP experiments by Rao *et al.* (2013, 2015, 2017). A vertical PHP tube of the inner diameter $d_i = 2$ mm and total length of 70 cm was made of borosilicate glass. The temperatures of both evaporator (T_e) and condenser (T_c) were regulated with an accuracy of ± 1 K by using glass heat exchangers connected to two thermostatic baths. The adiabatic section of the length $L_a = 1$ cm was transparent either. The evaporator and condenser lengths were equal, $L_e = L_c = 20$ cm (cf. Fig. 2). Different fluids were used (n-pentane, FC72, ethanol, de-ionized water). The temperature in the two-phase reservoir (liquid+vapor) was controlled due to the high-precision (± 0.2 K) thermostatic bath that regulated the fluid temperature and thus its saturation pressure. This experiment was repeated by Recklin *et al.* (2015).

It has been established that self-sustained oscillations do occur in such a simple system as a result of a thermo-mechanical instability. The oscillations are stable

and periodic (or, strictly speaking, quasi-periodic) over long periods of time. It was found that their occurrence is controlled not only by the difference $T_e - T_c$, but also by the absolute values of T_e and T_c . The vapor pressure oscillates around the pressure p_r^H in the reservoir corrected for the hydrostatic pressure contribution of the average liquid column height. Contrary to the naive idea of the vapor compression by the advancing liquid plug, the maximum of the vapor pressure p does not occur when the meniscus reaches its uppermost position in the evaporator. It occurs instead when the meniscus reaches the adiabatic section while *receding* from evaporator towards condenser. Rao *et al.* (2015) explained this phase shift by the fact that the vapor mass increase caused by the film evaporation contributed into the vapor pressure rise. It was possible to estimate indirectly the liquid film thickness, of the order of $70\ \mu\text{m}$.

Two types of oscillation regimes were observed. In the first regime (observed only in the historically first installation, that of Das *et al.* (2010) for large T_e), the meniscus penetrated the evaporator at each oscillation so the amplitudes of the sequential oscillations were equal. In the second regime, the meniscus did not penetrate into the evaporator each second oscillation.

2.2. Assessment of the vapor thermodynamic state

The vapor thermodynamic state is a key issue for the PHP theoretical description because the vapor plays a role of the spring that provides oscillations. On one hand, a naive idea on the vapor state comes from the analogy with the conventional heat pipes where the vapor is at saturation temperature T_{sat} , corresponding to its pressure p . On the other hand, the vapor can be superheated with respect to T_{sat} , i.e. it situates in the gas region of the fluid phase diagram (Fig. 3). To distinguish between these states, a single branch PHP experiment has been carried out by Gully *et al.* (2014). In the single branch PHP, the vapor bubble pressure is easy to

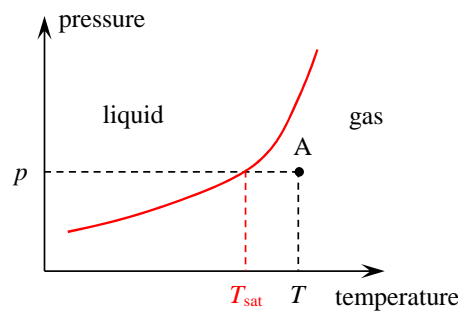


Fig. 3. Sketch of the saturation curve and regions corresponding to the liquid and gas phases. For a given pressure p , the thermodynamic state of saturated vapor with the temperature T_{sat} corresponds to the intersection of the horizontal dashed line with the saturation curve. The superheated vapor (or gas) thermodynamic state A with the corresponding temperature $T > T_{\text{sat}}$ (this is why it is called superheated) is shown with a black dot.

access because the vapor position is known in advance. The main objective of this experiment was the measurement of the transient vapor temperature T . This is not an easy task because of the weak heat exchange between a temperature sensor and the vapor. For this reason, it is important to get rid of the parasite heat fluxes coming to the sensor, in particular of the radiative heat exchange with the internal tube walls. To reduce this exchange, the experiment has been conducted with oxygen at about 70K. A microscopic thermocouple (μ TC) of diameter $30\ \mu\text{m}$ has been installed inside the vapor phase.

The results are presented in Fig. 4. The temperature $T_{\mu\text{TC}}$ measured by the

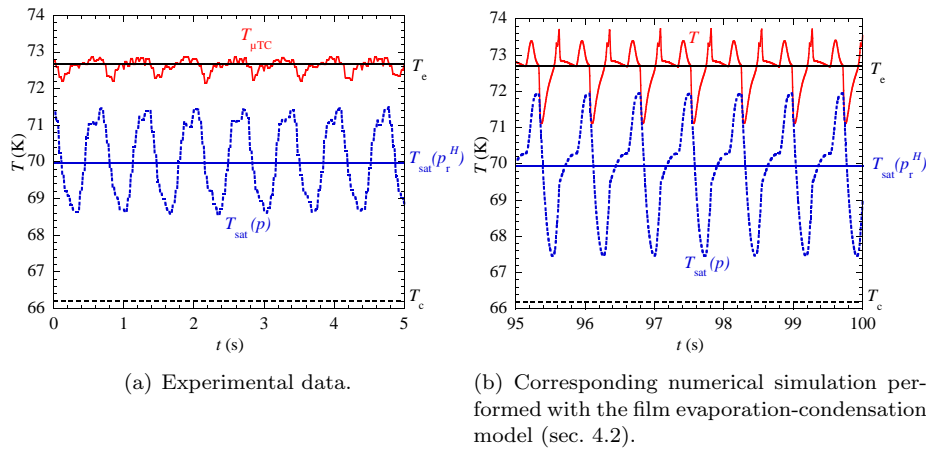


Fig. 4. Results of the cryogenic single branch PHP experiment and corresponding modeling [Gully *et al.* (2014)].

micro-thermocouple is compared to $T_{\text{sat}}(p)$ calculated from the measured evolution $p(t)$ of the pressure in the vapor bubble. Since the pressure oscillates around the pressure p_r^H , the saturation temperature oscillates around the constant value $T_{\text{sat}}(p_r^H)$. The μ TC measurements (Fig. 4a) reveal several important features. First, $T_{\mu\text{TC}}$ oscillates around the evaporator temperature T_e which shows the importance of heat exchange between the vapor and dry tube in the evaporator. Second, $T_{\mu\text{TC}}$ remains always larger or equal to $T_{\text{sat}}(p)$ which means that the vapor can always be considered as superheated (cf. Fig. 3). The most striking feature is that the vapor sometimes becomes hotter than the wall that heats it, which shows the importance of vapor compression. A comparison with the theoretical modeling (Fig. 4b) suggests that, in spite of substantial efforts to reduce the thermal inertia of the thermocouple, it probably does not resolve rapid temperature variations related to vapor compression or expansion.

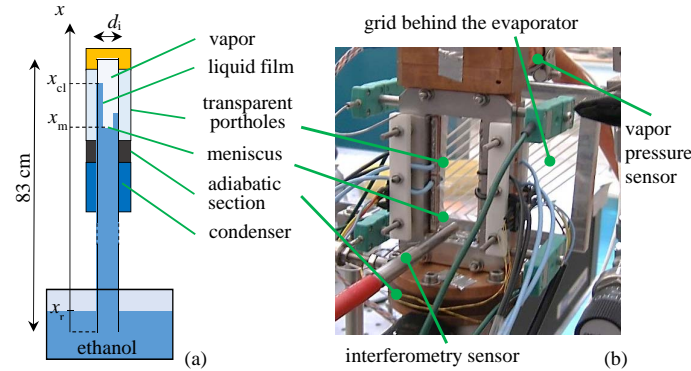


Fig. 5. (a) Sidewise scheme of the single branch PHP of Fourgeaud *et al.* (2017) and (b) a closer view of the PHP upper part (front view of evaporator and adiabatic section). The setup is backlit with the diffuse light and is filmed by a camera from the front.

2.3. Liquid film dynamics in evaporator

The primary importance of liquid films in the PHP tube is clear. Apart from their function as a major channel of heat and mass transfer like in the conventional heat pipes, the film evaporation/condensation provides a motor for the PHP oscillation. In the evaporator, the film thinning may lead to its localized drying so that its area changes and the triple liquid-vapor-solid contact line (CL) appears. It can move thus leading to a change of the total film area. Since the film area together with the film thickness are the most important issues for the PHP theory, one needs to study the CL dynamics.

To our knowledge, the first film observation has been made in the open U-turn water PHP [Lagubeau (2006)] (two branch PHP with the vapor bubble in the middle that works nearly like two single branch PHPs). Several film observations have been carried out since then [Hao *et al.* (2014); Rao *et al.* (2015); Srinivasan *et al.* (2015)]. The film length has been measured in the single branch PHP discussed above [Rao *et al.* (2015)]. The film length measurements have shown that the liquid film is indeed deposited by the receding liquid meniscus like in Taylor bubbles. Assessment of the film profile and thickness by direct measurements in the capillaries of the circular cross-section is problematic. The confocal microscopy [Srinivasan *et al.* (2015)] was shown to be inefficient for the cylindrical tubes. The film profile reconstruction based on the measurements of the spatial temperature distribution with the infra-red camera lacks precision either [Chauris *et al.* (2015)]. It is possible to measure only the film length by this method [Fischer *et al.* (2015)].

The PHP tube in a recent experiment [Fourgeaud *et al.* (2017)] designed specially for the liquid film studies was a two-dimensional capillary, i.e. a vertical tube of uniformly rectangular cross-section of high aspect ratio, $2 \times 22 \text{ mm}^2$ (Fig. 5a).

The upper (evaporator) part of PHP is formed by two transparent sapphire portholes (Fig. 5b). The transparent ITO (indium-tin oxide) layers are deposited

at each porthole (outside). They are conductive and may be heated independently with electric current. The evaporator is filmed with a video camera. A much higher heating power is applied to the rear porthole ITO so that the film on it disappears quickly and the front film (facing the camera) can be studied alone. The ethanol is used as the working fluid.

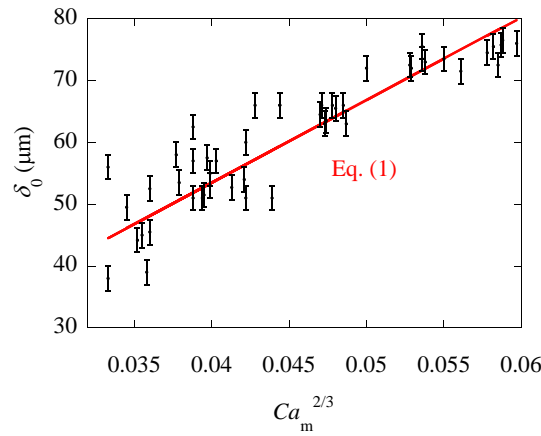


Fig. 6. Film thickness (characters with error bars) just after the film deposition as a function of the meniscus capillary number. It is compared to Eq. (1) (line) [Fourgeaud *et al.* (2017)].

First, Fourgeaud *et al.* (2017) verified that right after the liquid film deposition by the meniscus receding with the velocity V_m , its thickness δ_0 corresponds to the classical result [Bretherton (1961)] obtained for the Taylor bubble with no phase change. According to this theory, δ_0 is defined by the balance between the viscous friction force (that prevents the liquid from flowing along the solid) and the surface tension in the meniscus region that tends to keep all the fluid inside the plug. This balance results in the expression

$$\delta_0 = 0.67d_iCa_m^{2/3}, \quad (1)$$

where $d_i = 2$ mm is the spacing between the plates (Fig. 5a) and $Ca_m = \mu V_m / \sigma$ is the meniscus capillary number with σ , the surface tension, and μ , liquid shear viscosity. The measured by interferometry film thickness is presented as a function of Ca_m in Fig. 6. One can see that the measurements are coherent with Eq. (1). After the deposition, two phenomena occur to the film: its thinning and its contact line (CL) retraction. Both events are caused by evaporation, but in two distinctive film parts. While the CL retraction is controlled by the CL close vicinity, the film thinning occurs along all the film.

The film thickness δ measured at several fixed heights after the film deposition is shown in Fig. 7a. One can see that the film surface is inclined. However the film slope is weak, of the order of 0.6° (note the difference of the length scales of the vertical and horizontal axes).

To reconstruct stronger inclined film portions near the CL (Fig. 8), the grid deflection optical method is used. The first feature revealed by Fig. 8b is a finite value of the apparent contact angle that contrasts the complete wetting of sapphire by ethanol at equilibrium (Fig. 9). This phenomenon is discussed in sec. 3.3. The film thickness decrease from the meniscus to the ridge is only by the factor two (Fig. 7a). This shows that the constant thickness film assumed in the FEC model (sections 4.2, 6.2) is more adequate than the wedge-shaped film hypothesized by d’Entremont and Thome (sec. 6.4, see also Chapter 3) or Chauris *et al.* (2015). The wedge shape of the same slope would result in a much larger film length. To conclude this experimental part, the film shape in the PHP tube is sketched in Fig. 10.

3. Modeling of physical phenomena in the PHP “unit cell”

To understand theoretically the global PHP behavior, one needs to find out which phenomena occur locally in a single bubble-plug couple. In this section we will consider separately its different domains: liquid plug, vapor bubble and the liquid film (Fig. 10).

3.1. Fluid flow and heat exchange in the liquid domain

The main flow regime in the PHP is the slug flow often called “Taylor bubble” flow or “elongated bubble” flow, i.e. the flow of bubbles typically longer than the tube diameter d_i (Fig. 11a). There are many studies of constant speed flows of this type,

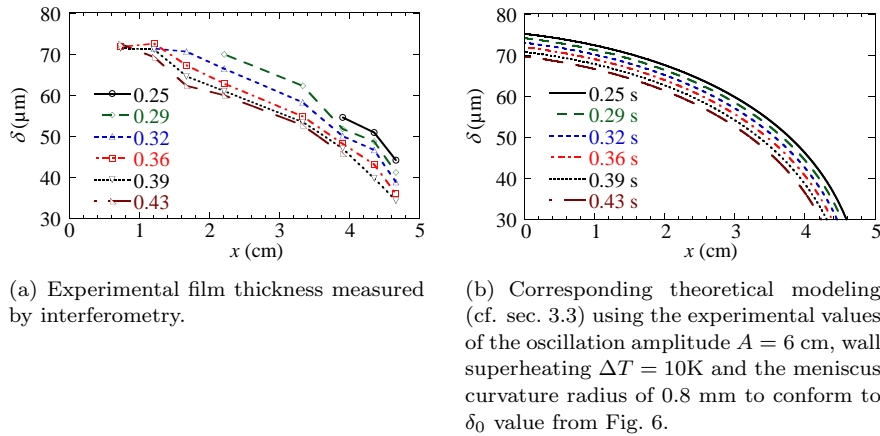


Fig. 7. Film thinning caused by evaporation measured for $p_r = 23.7$ kPa, $T_c = 0^\circ\text{C}$, and heating powers 4 and 60 W at the front and rear portholes, respectively, for the single branch PHP of Fourgeaud *et al.* (2017). Line captions show the time in seconds counted from the time moment of the topmost liquid meniscus position. The $x = 0$ point corresponds to the bottom of the camera view field.

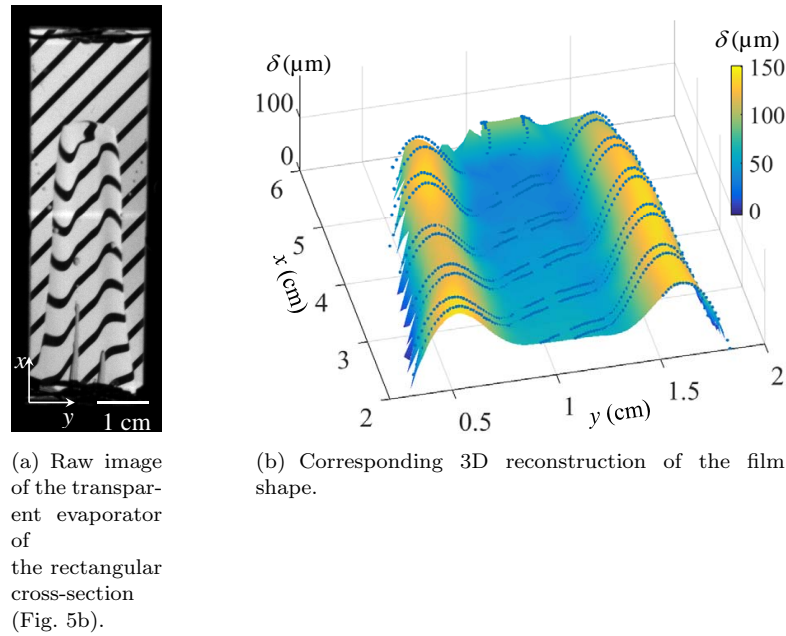


Fig. 8. Image of the film and its reconstructed shape. The 3D surface is obtained by interpolation between reconstructed points (dots) along the images of grid edges. Note that the lateral ridge parts appear because of the rectangular tube and the heating mode; they are absent in the circular tube PHP [Fourgeaud *et al.* (2016)].

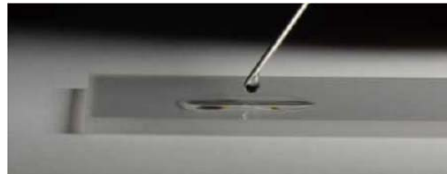


Fig. 9. Spreading of an ethanol droplet on the clean sapphire substrate at the ambient conditions [Fourgeaud (2016)] indicating nearly zero contact angle.

both theoretical, numerical, and experimental. These studies are driven mainly by the technological applications in microfluidics and chemical engineering and thermal engineering, for the flow boiling heat exchangers. Starting from the articles by Bretherton (1961), the studies concern the pressure drop and heat exchange rate as a function of flow rate and void fraction. An important issue, the liquid film modeling, will be addressed in sec. 3.3. Since, typically, the thickness of the films is much smaller than the tube diameter, the liquid flow is almost independent of their presence or absence.

Instead of discussing correlations for the pressure drop and heat exchange models that can be found in many reviews (see e.g. [Gupta *et al.* (2010); Talimi *et al.*

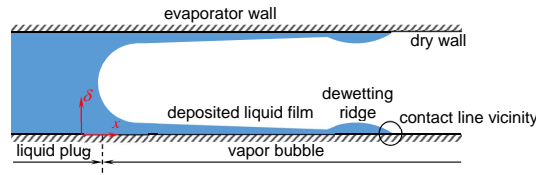
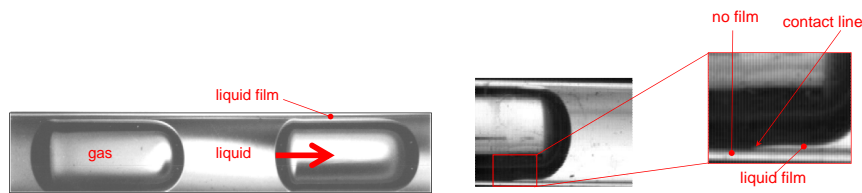


Fig. 10. Sketch of the film shape in the PHP evaporator. The ridge width is exaggerated for illustration sake.



(a) Classical Taylor bubble flow. The direction of fluid motion is indicated with an arrow. Note the difference of curvature of the leading (where the liquid recedes) and trailing (where the liquid advances) bubble menisci. The liquid film around each bubble is continuous.

(b) Vapor bubble in the cylindrical PHP tube [Lagubeau (2006)]. The tube wall is partly dried out and the triple vapor-liquid-solid CL is formed. Its vicinity is zoomed in.

Fig. 11. Difference of conventional Taylor bubbles and bubbles in PHP.

(2012); Wörner (2012); Baldassari and Marengo (2013)]), we will address here the main physical features of the flow and their impact. We will consider separately different aspects of this complicated issue. First we consider the Taylor bubble flow without phase change, typically, air bubbles in a liquid in isothermal case. Next, we discuss the hydrodynamics and heat transfer in the oscillating single-phase flow. Finally, the PHP-oriented research in this field, i.e., that involving the oscillating Taylor bubble flow with heat transfer, is discussed.

3.1.1. Isothermal Taylor bubbles

Let us start with the pressure drop for isothermal constant velocity Taylor bubble flow. It is related to the curvature of menisci and the flow pattern in the liquid plugs. The curvature defines the interfacial pressure jump. If the curvatures of the advancing and receding menisci of a bubble were equal, the contribution of the interfaces to the overall pressure jump would be zero. However, in reality the curvature of the leading meniscus is always larger than that of the trailing meniscus (cf. Fig. 11a), so the meniscus contribution to the overall bubble pressure drop is positive. According to Bretherton (1961), the pressure drop effect created because

of the curvature difference is

$$\Delta p_m = 14.89 C a_m^{2/3} \frac{\sigma}{d_i}. \quad (2)$$

In spite of the smallness of the Reynolds number $Re_m = V_m d_i / \nu$ (with $\nu = \mu / \rho$, liquid kinematic viscosity and ρ , liquid density) typical for narrow tubes, the plug flow pattern is not the parabolic Hagen-Poiseuille profile because of the menisci influence. Indeed, if one considers the reference in which the mass center of the liquid plug is immobile, the tube will move and drag the liquid. To provide the liquid mass conservation, the liquid velocity at the plug axis should be opposite, which means that a toroidal roll is created inside the plug (cf. above mentioned reviews for an extended discussion). The flow change with respect to the Hagen-Poiseuille profile is strong near the menisci but is small in the middle of the plug. Therefore, the viscous drag is expected to contain a contribution from this effect independent of the liquid plug length L_1 . According to Kreutzer *et al.* (2005), the overall pressure drop contains the Hagen-Poiseuille term and the L_1 -independent term that accounts of the both above effects:

$$\Delta p = \frac{64}{Re_m} \frac{\rho V_m^2}{2} \left[\frac{L_1}{d_i} + 0.17 \left(\frac{Re_m}{Ca_m} \right)^{1/3} \right]. \quad (3)$$

The numerical coefficient and the Re_m dependence provide both the best fit to experimental data for air bubbles in several liquids (in isothermal case) and numerical data.

As will be shown below, both the phase change and oscillations impact the curvature of menisci and the flow inside the liquid. The influence of these effects on the pressure drop is yet to be studied.

3.1.2. Pressure losses in the liquid phase

Consider a liquid motion induced by a periodical in time pressure variation with the angular frequency ω . Two main parameters are necessary for PHP modeling: the viscous friction force F acting on the liquid plug, and the heat transfer defined by the Nusselt number. These two issues will be considered separately. The liquid is considered to be incompressible which is, clearly, a valid approximation in PHP (the oscillation frequency is limited by the liquid plug inertia and thus remains much smaller than the sound velocity).

To evaluate F , one needs to know the shear stress

$$\tau = \mu \frac{\partial u_x}{\partial n} \quad (4)$$

at the tube wall, where \vec{n} is the internal normal to the wall (cf. Fig. 12) and u_x is the tangential component of the liquid velocity. The force F is then equal to τ integrated over the wall area covered by the liquid plug. The shear rate should be

expressed in terms of the plug velocity V that corresponds to the liquid velocity averaged over the tube cross-section. For the circular tube,

$$V = \frac{8}{d_i^2} \int_0^{d_i/2} u_x(r) r dr. \quad (5)$$

For the liquid flow, the relevant length scales are the tube diameter (or the plate spacing in the case of a slot) d_i and the amplitude A of the liquid displacement along the tube axis. The relevant scale $\delta_S = \sqrt{2\nu/\omega}$ is called Stokes length. Its physical meaning will be explained below. One can thus introduce their combinations, the Womersley number

$$Wo = \frac{d_i}{2} \sqrt{\frac{\omega}{\nu}} \quad (6)$$

and the transition number

$$\beta = 2A\sqrt{\omega/\nu} \quad (7)$$

used to define the transition from laminar to turbulent flow that occurs when β attains a value close to 700 [Zhao and Cheng (1996)]. The PHP flow is usually below this limit, hence we will consider hereafter only the laminar case. In the

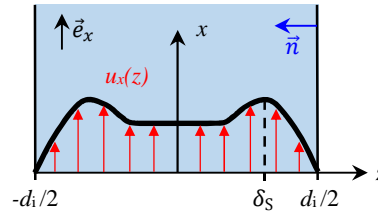


Fig. 12. Sketch of the laminar oscillating flow pattern. The profile corresponds to the averaged in time root mean square velocity.

laminar flow (Fig. 12), the liquid velocity \vec{u} is parallel to the tube direction defined by the unit vector \vec{e}_x , $\vec{u} = u_x(z)\vec{e}_x$. Evidently, the advection term $(\vec{u} \cdot \nabla)\vec{u}$ (with ∇ the gradient vector operator) vanishes and the Navier-Stokes equation reads

$$\rho \frac{\partial u_x}{\partial t} = -\frac{\partial p_1}{\partial x} + \mu \nabla^2 u_x, \quad (8)$$

where t is the time.

Let us first describe qualitatively the liquid flow pattern (Fig. 12). During oscillations, a boundary layer of the thickness δ_S develops if it is small with respect to the tube diameter (i.e. for $Wo \ll 1$) and the bulk fluid oscillates as a block [Schlichting (1968)], with $\pi/2$ phase shift with respect to the pressure. Maxima of velocity u_x occur at a distance $\sim \delta_S$; this phenomenon is referred to as the Richardson annular effect.

Eq. (8) is linear and can be solved by Fourier transform over time by applying the no-slip boundary condition

$$u_x = 0 \quad (9)$$

at the solid walls (Fig. 12). For the circular tube, the $\tilde{u}_x(z)$ solution [Schlichting (1968)] results in the following expression

$$\tilde{\tau} = \frac{\mu\chi\tilde{V}}{\frac{I_0(\chi d_i/2)}{I_1(\chi d_i/2)} - \frac{4}{\chi d_i}}, \quad (10)$$

where I_0 is the modified Bessel function, tilde means the Fourier transform, i is the imaginary unit and $\chi = \sqrt{\frac{i\omega}{\nu}}$. In the limit $\omega \rightarrow 0$, this expression reduces to the Hagen-Poiseuille result

$$\tau = 8\mu V/d_i \quad \text{and} \quad F = 8\pi\mu V L_1. \quad (11)$$

In some cases the flow can become turbulent; the expression

$$F = C\pi r_i \rho V^2 L_1 \text{sign}(V) \quad \text{with} \quad C = \begin{cases} 0, & Re = 0 \\ 16/Re, & 0 < Re_i < 1180 \\ 0.078Re^{-0.25}, & Re \geq 1180 \end{cases} \quad (12)$$

was used in many PHP simulations following Shafii *et al.* (2001), with $Re = |V|d_i/\nu$. The second line of this equation corresponds to the expression (11).

To obtain the equation of motion of liquid plug, one needs to integrate Eq. (8) over the tube cross-section S and plug length L_1 . The result is [Nikolayev (2011b)]

$$\frac{d}{dt}(m_l V) = (p - p_{\text{next}})S - F - F_{\text{turn}} + G, \quad (13)$$

where the l.h.s. term is simply the plug momentum change per second, $m_l = L_1 S \rho$ the plug mass, G , the gravity force, and F_{turn} , a supplementary force coming from the pressure drop when the entire plug or its any part enters inside the curved part of tube. The pressures p and p_{next} correspond to the ends of the plug (“next”, in the direction of the x axis).

The pressure loss in the PHP tube turns may be important. However even the single phase flow remains to be an open problem in the presence of oscillations. We discuss here the results for constant V . The F_{turn} term was first introduced into the PHP modeling by Mameli *et al.* (2012) using the 3-K Darby method [Darby and Chhabra (2017)] for its calculation. In PHP, only a part of the liquid plug of the length $L_{l,\text{turn}} < L_1$ may be present in the tube bend. The turn angle $\varphi = L_{l,\text{turn}}/r_{\text{turn}}$ of the plug (where turn radius r_{turn} is measured along the tube axis line) may vary and be different from the discrete values 90° or 180° considered by Darby. For this reason, the following approach seems to be more appropriate for

the PHP case. Idelchik (2008) defines the additional resistance force (in fact of the inertial origin) as

$$F_{\text{turn}} = \frac{1}{2} S \rho V^2 A_1(\varphi) B_1(r_{\text{turn}}/d_i) \text{sign}(V) \quad (14)$$

where the $A_1(\varphi)$ function is nonlinear

$$A_1(\varphi) = \begin{cases} 1, & \varphi = \frac{\pi}{2}, \\ 0.9 \sin \varphi, & \varphi < \frac{7}{18}\pi, \\ 0.7 \left(1 + \frac{\varphi}{\pi}\right), & \varphi > \frac{10}{18}\pi. \end{cases} \quad (15)$$

As for the B_1 term, in the most common case $r_{\text{turn}} > d_i$,

$$B_1 = 0.21 \sqrt{\frac{d_i}{r_{\text{turn}}}}. \quad (16)$$

Such an approach was used in the simulation of Nekrashevych and Nikolayev (2017).

The heat exchange in oscillating single phase flow has been actively since a work of Kurzweg and de Zhao (1984) who developed an analytical approximate theory. We note the works [Zhao and Cheng (1995); Li and Yang (2000); Hemida *et al.* (2002); Yu *et al.* (2004); Yin and Ma (2014)]. Most of these studies were reviewed recently by Ma (2015). It has been shown that the Nusselt number varies around the unidirectional laminar flow value $Nu_1 = 4.36$, but the variation is small, so this value appears to be a good approximation. This data has also been confirmed experimentally in a square channel by Mehta and Khandekar (2015).

3.1.3. Taylor bubbles under pulsations and heat transfer

In PHPs, the elongated bubbles are submitted to both oscillating pressure and heat transfer conditions. Most of the work on the elongated bubbles heat transfer under constant flow conditions has been carried out in relation with flow boiling. One can mention reviews of simulation results by Gupta *et al.* (2010); Talimi *et al.* (2012). Among more recent studies, one notes those of Magnini *et al.* (2013a) who simulated the motion of elongated bubbles combined with their growth due to the film evaporation. The continuous film case (cf. Fig. 11) has been considered. It has been verified that the bubble volume grows mainly due to the film evaporation.

The fluid flow in PHP is difficult to be studied; for this reason its understanding is still very incomplete, cf. Khandekar *et al.* (2010) for a review. It has been found out that the meniscus curvature changes strongly depending on the direction of its motion (advancing or receding) and on the velocity [Lips *et al.* (2010)]. This effect is equivalent to variation of the apparent contact angle θ_{app} (will be discussed later in sec. 3.3). By postulating θ_{app} dependence on the plug velocity, both the liquid flow and heat transfer inside a plug moving in a dry capillary (no film at all) with a constant velocity have been analyzed numerically by Bajpai and Khandekar (2012) for several fluids. They used two kinds of boundary conditions at the internal tube wall: constant temperature and constant heat flux. We will discuss here the constant

temperature condition that seems to be more realistic. A strong heat exchange has been found in the meniscus regions of the plug that provided overall heat transfer enhancement for short plugs. This enhancement has been attributed to the toroidal vortex discussed in sec. 3.1.1. The Nusselt number grows with the plug velocity and can attain ~ 40 for short water plugs ($L_1 = d_i$) for $Ca_m = 10^{-3}$. The Nu value decreases with the plug length increase and approaches the above discussed 4.36 value in the limit of a very long plug. Since the advancing and receding θ_{app} are different, the toroidal vortex inside the plug is asymmetrical, which improves the heat transfer. Similar results (although discussed in terms of neighboring bubble interaction through the liquid plug) are obtained by Magnini *et al.* (2013b) who simulated the case of continuous liquid film inside the bubbles.

To our best knowledge, there are no local heat transfer studies for Taylor bubble flow under oscillation conditions up to now. A study of the *pulsating* Taylor bubble flow with heat exchange has been carried out by Mehta and Khandekar (2014). The fluid flow was unidirectional, with the imposed volume flow rate changing periodically from zero to a maximum. The Taylor bubbles were generated by injection of air into the water flow. The generated bubble train passed through a transparent section for visualisation and then to a copper heated section filmed with the infrared (IR) camera. The constant volume flow rate case has been compared to the pulsating flow case with the same average flow rate. It should be noted that such an experiment evaluates mainly the liquid-wall heat exchange. Unlike the vapor bubble case where the film evaporation provides a heat sink [Chauris *et al.* (2015)], the heat exchange with the air bubble-covered area of the wall has been observed to be very weak. A spatial variation in the liquid-wall heat exchange rate has been observed along the liquid plug-covered area of the wall. The heat exchange was stronger near the meniscus than in the plug bulk. This finding agrees with numerical simulations [Bajpai and Khandekar (2012)] on constant velocity flow. It has been found that the heat exchange increased with the frequency of pulsations. An increase of the average heat exchange rate ($Nu \simeq 8$) has been encountered.

Another study of the oscillating Taylor bubble flow with heat exchange has been carried out by Pattamatta *et al.* (2015) who performed a direct numerical simulation of air bubbles in FC72 with no phase change. The simulations have shown the films of variable thickness (wavy shape) which can probably be understood as a result of propagation of disturbances appearing near the menisci during their oscillation (cf. Fig. 15 and associated discussion). The conclusions of the heat transfer studies are similar to those of Mehta and Khandekar (2014).

3.2. Physics and modeling of vapor phase

In a physical system exhibiting oscillations there is always an elastic agent that provides a restoring force while it is compressed or dilated. It is clear that in PHP, this role can be played only by the vapor. For this reason, the vapor thermodynamic state is probably the most crucial issue for the reliable PHP modeling. In their

pioneering article on the PHP modeling, Shafii *et al.* (2001) assumed that the vapor behavior may be assimilated to that of the ideal gas that is described by the equation of state (EOS)

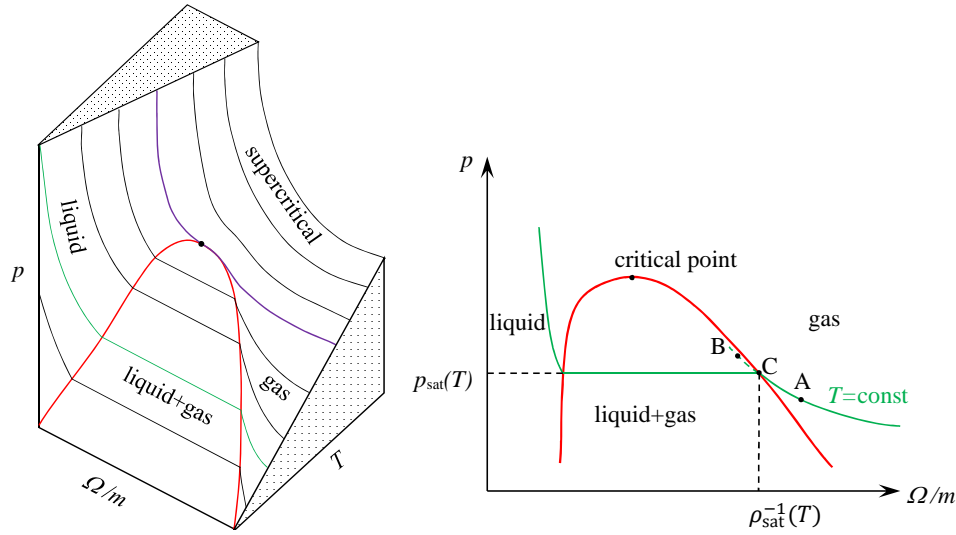
$$p = mR_v T / \Omega, \quad (17)$$

with m , the vapor mass, T , its temperature, Ω , its volume, and R_v , the vapor gas constant. At the same time, one needs to introduce the phase change. In their model, Shafii *et al.* (2001) assumed that the phase change rate is proportional to the difference $T_w - T$ of tube wall and vapor temperatures. The same assumption has been adopted later by Dobson (2004); Holley and Faghri (2005) and more recently by many other authors [Sakulchangsattajai *et al.* (2008); Givler and Martinez (2009); Yuan *et al.* (2010); Shao and Zhang (2011); Cheng and Ma (2011); Mameli *et al.* (2012); Ma (2015); Manzoni *et al.* (2016b)]. This assumption has been justified by Zhang and Faghri (2002) by the fact that the evaporation flux is provided by the film evaporation/condensation which is well known to be proportional to the $T_w - T_{\text{sat}}$ (cf. sec. 3.3). Zhang and Faghri postulated that the vapor is at saturation so, according to them, $T = T_{\text{sat}}$, which justified the phase change rate proportional to $T_w - T$.

This assumption however is in an apparent contradiction with Eq. (17). Indeed, the pressure of saturated vapor is entirely defined by its temperature with the saturation curve (Fig. 3) rather than by Eq. (17). In addition, for a particular case of the experiment described in sec. 2.2, $T > T_{\text{sat}}$ has been measured. Because of this confusion and the importance of this question, the vapor thermodynamic state is discussed below starting from basics.

3.2.1. Vapor thermodynamic state

Consider first the equilibrium state, to be distinguished from the metastable state considered next. A very general phase diagram for a single component fluid at equilibrium is sketched in Fig. 13a. The fluid equation of state (EOS, i.e. the set of thermodynamic states that can be occupied by the fluid) is a surface in the coordinates (p, Ω, T) . The two phase (liquid-gas) coexistence region situates inside the red bell-shaped curve called coexistence curve. A part of the surface inside this curve is parallel to the volume axis so its projection to the $p - T$ plane is just a line called saturation curve shown in Fig. 3. A part below the saturation curve corresponds to the gas phase (in which point A is situated), a part above, to the liquid. The same point A is represented in Fig. 13b. Every state inside the coexistence region is a mixture of the liquid and gas with the saturation densities given by the coexistence curve. This is illustrated in Fig. 13b, which is a projection of the surface of Fig. 13a to the pressure-volume plane. The saturated vapor specific volume ρ_{sat}^{-1} corresponds to the point C. In the gas region, the exact vapor EOS approaches closely the ideal gas EOS (17). For this reason, there is no need to use more sophisticated EOS forms.



(a) Phase diagram in the coordinates pressure-volume-temperature. The surface corresponding to the EOS is shown with the curves corresponding to constant temperature values (isotherms).

(b) Projection of the surface shown in (a) to the pressure-volume plane.

Fig. 13. Schematized phase diagram of a fluid.

Instead of using EOS (17), d'Entremont and Thome (2015a,b) assumed the vapor to always remain at saturation evolving along the gas branch of coexistence curve (part of the red curve in Fig. 13b to the right of the critical point). During the volume variation (vapor compression/dilatation) due to oscillations, vapor density ρ_{sat} changes and they find the new vapor temperature by using the $\rho_{\text{sat}}(T)$ curve. We note that the saturated vapor model also creates a kind of elastic response: when the vapor volume reduces at constant mass, ρ_{sat} increases (i.e. ρ_{sat}^{-1} decreases) and the pressure rises according to Fig. 13b together with the vapor temperature. Note that the such an “automatic” temperature change at compression/dilatation is hardly justified because the associated vapor energy change is not balanced. In a more realistic model, the vapor temperature change should be defined from the vapor energy balance that includes the heat exchange with environment, see sec. 3.2.2.

A fundamental difference between the saturated vapor (corresponding to the point C in Fig. 13b) and the gas state (called also superheated vapor, point A) is evident now. Because of this difference, the vapor cannot be simultaneously and continuously both at saturation and gas states, contrary to what was assumed by Shafii *et al.* (2001) and their followers.

Let us consider now what happens in a real fluid on an example of the vapor

isothermal volume reduction (i.e. compression). When the saturated vapor is compressed slowly, condensation occurs and the point C displaces along the horizontal line inside the coexistence region and no pressure rise necessary for the oscillation is generated. However, such a process requires a strong and slow compression so liquid drops have time to be nucleated and the energy excess is high enough to overcome the nucleation barrier [Carey (1992)]. When the vapor is compressed fast enough and its compression is not strong, the nucleation does not occur and the vapor evolves into a metastable state (point B). In PHP visualization experiments, the mist-like condensation characteristic for the nucleation scenario was never observed which shows that the metastable scenario holds. In both cases, such a picture is contrary to the assumption according to which the vapor always remains at saturation.

When the superheated vapor is compressed or dilated, the point A moves along the isotherm and the pressure changes, which creates a restoring force for the oscillation. Such a model has been confirmed experimentally. The experiment described in sec. 2.2 has shown that the vapor superheating can be of the order of 10K. The same experiment has shown that the vapor is nearly always superheated so it never comes to a metastable state. To manage rare metastability events in the modeling, a solution proposed by Shafii *et al.* (2001) can be used: the pressure is imposed to be p_{sat} , i.e. the point B is shifted artificially to the point C.

The vapor temperature is not entirely homogeneous during vapor compression or expansion. Thermal boundary layers are developed near both the tube walls at temperature T_w and the liquid films at temperature T_{sat} covering the walls. The thickness of these layers is a complex yet unsolved issue. Direct numerical simulations [Gully *et al.* (2014)] of the gas flow during oscillatory compression performed with ANSYS CFX software for oxygen at about 70K showed a thickness of ~ 0.25 mm in the tube of 2 mm diameter. The vapor flow remains mostly laminar in the thermal boundary layers; turbulent mixing is absent near the wall. For this reason, in one-dimensional models one can reasonably assume that the vapor bulk can be described by a unique temperature. Because of a large temperature difference, the vapor heat exchange is mainly that with the dry wall area of the length L_d . The heat exchange coefficient is $U_v = Nu_v \lambda_v / d_i$ and the heat exchange rate is

$$\dot{Q}_v = U_v \pi d_i L_d (T_w - T). \quad (18)$$

The above numerical calculation resulted in $Nu_v \simeq 6$.

3.2.2. Vapor energy equation

The vapor energy equation depends on the vapor thermodynamic state and should be derived from the first law of thermodynamics. When the vapor is superheated and obeys the ideal gas law (17), Shafii *et al.* (2001) showed that it can be described by the equation (see [Nikolayev (2011a)] for its detailed derivation)

$$mc_{vv}\dot{T} = R_v T \dot{m} - p\dot{\Omega} + \dot{Q}_v \quad (19)$$

where c_{vv} is the vapor heat capacity at constant volume and dot means the time derivative. If one neglects \dot{Q}_v , this equation can be reduced by using both EOS (17) and Mayer's relation $c_{pv} = c_{vv} + R_v$ valid in the ideal gas approximation:

$$\frac{\dot{T}}{T} = \frac{\gamma - 1}{\gamma} \frac{\dot{p}}{p}, \quad (20)$$

where $\gamma = c_{pv}/c_{vv}$ is the adiabatic index. The advantage of this representation is that it can be integrated directly resulting in the form with no explicit dependence on time [Zhang *et al.* (2002)],

$$p \sim T^{\frac{\gamma}{\gamma-1}}. \quad (21)$$

This approximation is convenient because reduces a number of differential equations that need to be solved numerically. For each bubble, instead of solving the differential equation (19), one uses the expression (21). Such an approach was used by several authors. The neglected energy transfer \dot{Q}_v to the vapor is generally smaller than the axial heat transfer (and can be indeed neglected) when calculating the overall heat transfer in the stable oscillation regime. However, in the vapor energy balance \dot{Q}_v is important. In particular, it will be shown in sec. 4.5 that \dot{Q}_v term is essential for the start-up threshold determination.

There was (and still is) a lot of controversy concerning the vapor energy equation beginning with the work of Dobson (2004) who replaced $R_v T$ in Eq. (19) by the vapor enthalpy h_v . This is obviously incorrect because h_v is defined within an arbitrary constant, see Nikolayev (2011a). An incorrect by the same reason energy equation

$$\frac{d}{dt}(h_v m) = \dot{Q}_v$$

was used in a multi-branch PHP simulation by Holley and Faghri (2005) and later by Mameli *et al.* (2012), and, in a different, but similar form, by Manzoni *et al.* (2016b,a). In other words, $R_v T$ in Eq. (19) was replaced by a much larger (for water, 10 times larger) quantity h_{lv} , which means an overestimation of the power injection into the vapor and thus an overestimation of its mechanical response. Instead of being injected into the vapor, the latent heat released in film condensation goes in reality directly to the condenser portion of the tube wall through more conductive liquid films onto which condensation occurs preferentially (cf. Eq. (24) below).

Another example of the incorrect vapor energy balance is a recent work [Gürsel *et al.* (2015)] where the vapor is treated as if it were solid ($mc_{pv}\dot{T} = \dot{Q}_v$), with nor pressure work neither phase change account.

3.3. Liquid films in PHP

In this section we explain theoretically the film shape pictured in Fig. 10 by considering separately each part of the film. First we consider the extended part of the film.

3.3.1. Liquid film deposition by receding meniscus

The liquid films in PHP are entirely different from their counterparts in capillary heat pipe. In the latter, the films appear because of wetting, i.e. because of the intermolecular (van der Waals) attraction forces often described in terms of disjoining pressure. While the typical thickness scale for wetting films is 10-100 nm, the thickness of PHP films is much larger, 10-100 μm (sec. 2.3). For this reason, the description of PHP films [Zhang and Faghri (2002); Shao and Zhang (2011)] in terms of the disjoining pressure is not adequate. The liquid films in PHP are of purely hydrodynamic origin and appear as a result of receding of a liquid meniscus almost independently of the wetting properties of the tube wall (their length however does depend on the wetting properties as will be discussed below). The PHP film remains however thin enough so its Reynolds number remains very small (typically, $Re_f \sim 10^{-3}$).

As mentioned before, the PHP films have the same origin as the film deposited by the leading meniscus of Taylor's bubble (Fig. 11a). The liquid film appears as a result of competition between the viscous and capillary forces in a transition region adjacent to the liquid meniscus. The viscous friction tends to immobilize the fluid near the tube wall and thus to increase the film thickness. The surface tension tends to decrease the meniscus area thus making its radius of curvature as large as possible, which causes reduction of the film thickness. Such a competition is described with the meniscus capillary number Ca_m that defines the film thickness via Eq. (1) derived within an assumption $\delta_0 \ll d_i$. The film profile in the transition region from flat film to the spherical meniscus (Fig. 14a) can be determined by solving the fluid flow problem in the lubrication approximation [Bretherton (1961)]. Eq. (1) was corrected later to account for different effects like finiteness of δ_0/d_i ratio [Aussillous and Quéré (2000)], finiteness of the meniscus Reynolds number [Shikazono and Han (2011)], and acceleration of menisci [Han and Shikazono (2010)]. However the leading velocity dependence is defined by Eq. (1) in all the cases.

It is important to mention that the film deposition depends on the wetting properties of the capillary. For small contact angles, the films are always deposited because, when the receding motion begins, the CL is easily pinned at surface defects and the film forms immediately. For large contact angles, the film is deposited for $Ca_m \gtrsim 10^{-2}$, i.e. above the dynamic wetting transition [Delon *et al.* (2008)]. Receding of meniscus with no film discussed by Khandekar *et al.* (2010) is rarely encountered in PHP because Ca_m is large enough and the tube is generally well wetted by the liquid. The CL motion in this case obeys the same law as the film edge dynamics (sec. 3.3.5).

3.3.2. Meniscus motion over the preexisting film

Consider first the liquid meniscus advancing with a constant velocity V_m over the film of the thickness δ_0 . This is a situation of e.g. the rear meniscus of the Taylor

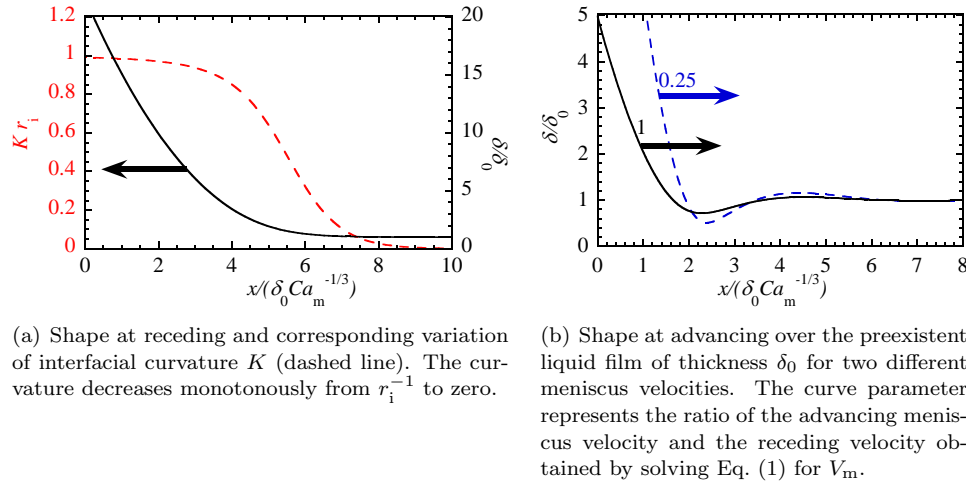


Fig. 14. The liquid-vapor interface shape $\delta(x)$ in the transition region between the flat liquid film and the spherical meniscus; axial cross-section of the tube is shown. The reference system is indicated in Fig. 10 in red. Zero of x axis is chosen arbitrarily. Arrows indicate the direction of meniscus motion [Nikolayev and Sundararaj (2014)].

bubble (Fig. 11a). One can see that the interface shape in the transition zone from the film to the spherical meniscus part in this case is wavy. Such a shape is often called “capillary shock”. To understand its origin, let us consider the Laplace equation that links the liquid pressure p_l at the liquid-vapor interface to its local curvature K

$$\Delta p \equiv p - p_l = \sigma K. \quad (22)$$

From the Navier-Stokes equation (8), the fluid flow direction is that of $-\partial p_l / \partial x$. According to Eq. (22), this quantity is equal to $\sigma \partial K / \partial x$ because the vapor pressure p is independent of x . For this reason, the monotonously decreasing curvature is incompatible with the positive flow direction created by the advancing meniscus. A wavy shape (i.e. changed by sign $\partial K / \partial x$) is needed to match them (Fig. 14b).

The interfacial shape depends on the velocity of the meniscus advancing. When the Taylor bubble velocity is constant, the velocities of the trailing and leading menisci are exactly equal. This situation corresponds to the curve labeled 1 in Fig. 14b. As an example, consider now the Taylor bubble deceleration. At a given x position, first the leading bubble meniscus passes and deposits a film of the thickness δ_0 corresponding to its instant velocity V_m^{rec} through Eq. (1). When the trailing (advancing) meniscus reaches x some time later, its velocity $V_m^{\text{adv}} = -V_m$ is smaller. The interfacial shape changes, cf. Fig. 14b, where the cases $V_m^{\text{adv}} / V_m^{\text{rec}} = 1$ and 0.25 are compared.

If the oscillation period $2\pi/\omega_0$ is much larger than the interface relaxation time $\delta_A \mu \sigma^{-1} Ca_A^{-4/3}$ (with $\delta_A = 0.67 d_i Ca_A^{2/3}$) the meniscus shapes during advancing

and receding phases correspond to their constant velocity counterparts as those of Figs. 14. In the opposite case, the wavy shape can propagate along the film (Fig. 15) so it persists during both advancing and receding phases of motion.

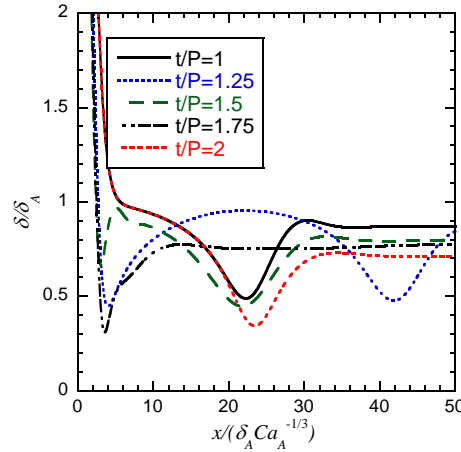


Fig. 15. Meniscus shape variation over one period (0.5s) of oscillations with the amplitude $A = 1$ cm for the case of ethanol at evaporation ($\Delta T = 5\text{K}$, the flat film portion thins with time) [Nikolayev and Sundararaj (2014)]. Time is shown as a fraction of oscillation period.

3.3.3. Liquid films at phase change

In the absence of phase change, a portion of the deposited film between the meniscus and the CL region remains to be of constant thickness. This occurs because of the absence of liquid flow in the film: there is no force inducing its motion. In the presence of phase change, the situation is different. While the flow along the film is still nearly absent, the film thins because of evaporations or thickens if condensation occurs. The thickness of the film portion deposited earlier changes with respect to that deposited later so the interface becomes inclined.

To evaluate this effect, one can neglect the flow along the film so the film thickness $\delta(x, t)$ changes because of phase change alone. The mass conservation at the interface implies that

$$\rho \dot{\delta} = -J, \quad (23)$$

where J is the mass evaporation flux. To obtain the film shape, consider the energy balance at the film surface. Its temperature T^i is (nearly always) equal to the saturation temperature T_{sat} corresponding to the vapor pressure because the fluid is pure. An exception to this rule is a microscopic vicinity of CL where the evaporation fluxes are very large, cf. Eq. (33) below. By neglecting the heat flux in the vapor with respect to the latent heat exchange, one can write the energy balance as

[Nikolayev (2010); Nikolayev and Sundararaj (2014)]

$$h_{lv}J = \frac{\lambda(T_w - T^i)}{\delta}, \quad (24)$$

where the right hand side is the heat flux arriving from the liquid side of the interface with λ , the liquid thermal conductivity, and h_{lv} , the latent heat. In the above expression, the stationary linear temperature distribution across the film is assumed. In the case of poorly conductive tube (plastic or glass), this approximation may be invalid, and the transient temperature distribution needs to be calculated [Rao *et al.* (2017)]; this is however unnecessary in a more common case of metal tube and non-metal fluid.

The discussion below will be limited to evaporation because of its importance (at film thinning, the phase change rate strongly increases).

The slope of evaporating film was introduced by several groups, e.g. by Thome *et al.* (2004); Chauris *et al.* (2015). They however assumed the wedge-shaped film, the thickness of which becomes very small near CL, which is not the case in PHPs (see sec. 2.3). By combining Eqs. (23) and (24) and by assuming a constant in time $\Delta T = T_w - T_{\text{sat}}(p)$ (i.e. an isothermal evaporator wall due to its high heat conductivity and constant vapor pressure), one gets a closed form equation for δ that solves to

$$\delta(x, t) = \sqrt{\delta_0^2 - 2 \frac{\lambda \Delta T}{h_{lv} \rho} [t - t_0(x)]}, \quad (25)$$

where $t_0(x) < t$ is the time moment of the meniscus passage through the point x . The function $t_0(x)$ is obtained by inversion of the meniscus motion law $x = X_m(t_0)$. The thickness $\delta_0 = \delta(t = t_0)$ is given by Eq. (1), which depends on $V_m = \dot{X}_m(t_0)$. Fig. 7b is obtained by using Eq. (25) and by assuming the harmonic meniscus oscillation [Fourgeaud *et al.* (2017)]. It is evident from the dimensional analysis that the film slope is controlled by the dimensionless parameter $\lambda \Delta T / (h_{lv} \rho |V_m| \delta_0)$ where $V_m < 0$ is the *receding* velocity. The slope increases with the wall superheating and decreases with the velocity: for a larger velocity the time to create the slope is smaller.

3.3.4. Contact line dynamics in the absence of the phase change

As mentioned above, the liquid film rupture can occur in PHP and the triple liquid-vapor-solid contact line (CL) appears. It can move (advance or recede), which is a process required to be modeled theoretically. However the flow generated by the CL motion cannot be explained in a framework of a conventional fluid mechanics approach where the Navier-Stokes equations are solved with the no-slip boundary condition (9). Indeed, CL belongs both to the liquid and to the solid and cannot move when the no-slip condition is applied. This phenomenon is frequently referred to as the CL hydrodynamic paradox. To solve it, an additional microscopic scale

mechanism (important in the CL vicinity) should be introduced into the theory. There are two common ways of theoretical solution of this paradox depending on the wetting properties. In the case of complete wetting of the solid by the liquid, the intermolecular (van der Waals) forces become dominant at small scales. It is convenient to describe them in terms of the disjoining pressure $\Pi(\delta) = H/(6\pi\delta^3)$. The Hamaker constant H is positive for complete wetting, and its typical value is about $10^{-20} - 10^{-19}$ J. The disjoining pressure enters the Laplace equation (22),

$$\Delta p = K\sigma + \Pi(\delta) \quad (26)$$

Due to a large value of Π at small δ , Eq. (26) describes a continuous wetting film covering the solid and connected to the liquid meniscus. The actual triple contact liquid-vapor-solid does not exist any more so its paradox does not occur. The film thickness scales on the Israelachvili length $l_I = \sqrt{H/(6\pi\sigma)}$ which is usually ~ 10 nm. Same situation occurs in the pseudo-partial wetting case where $H > 0$ like for complete wetting but the equilibrium contact angle defined from the surface energies through the Young expression is non-zero (see Brochard-Wyart *et al.* (1991) for the classification of wetting regimes).

For more relevant for PHPs partial wetting regime, the most common solution of hydrodynamic CL paradox is an account of hydrodynamic slip length l_s , i.e. replacement of the condition (9) by

$$u_x = l_s \frac{\partial u_x}{\partial n}. \quad (27)$$

Physically it means admitting a possibility for the liquid molecules to slip along the solid wall with a velocity proportional to the shear stress τ given by Eq. (4). Since the slip length is typically nano-scale [Lauga *et al.* (2007)], the right hand side differs from zero in a region where τ is very large, which occurs typically only very close to CL.

In both mechanisms of singularity relaxation discussed above, the CL vicinity influenced by these microscopic effects (called microscopic region, see is very small with respect to the macroscopic (i.e. millimetric) scale shown in Fig. 16c observable experimentally. It can be proved mathematically (cf. Snoeijer and Andreotti (2013) for a review) that the hydrodynamic flow generated at the intermediate length scales (say, in between 100 nm and 10 μ m from CL, Fig. 16b) is independent of the above microscopic effects. In fact they influence the intermediate region through a boundary condition at a scale ℓ_V (called Voinov length) corresponding to the size of microscopic region. This boundary condition is the equality of the interface slope $-\partial\delta/\partial x$ to θ_V (Voinov angle). Such an approach results in the Cox-Voinov law

$$\left| \frac{\partial\delta}{\partial x} \right|^3 = \theta_V^3 - 9Ca_f \log \frac{X_f - x}{\ell_V} \quad (28)$$

where X_f is the CL coordinate and $Ca_f = \mu V_f/\sigma$ is the CL capillary number involving with CL velocity V_f defined to be positive at receding. The Cox-Voinov law defines the slope in the intermediate region.

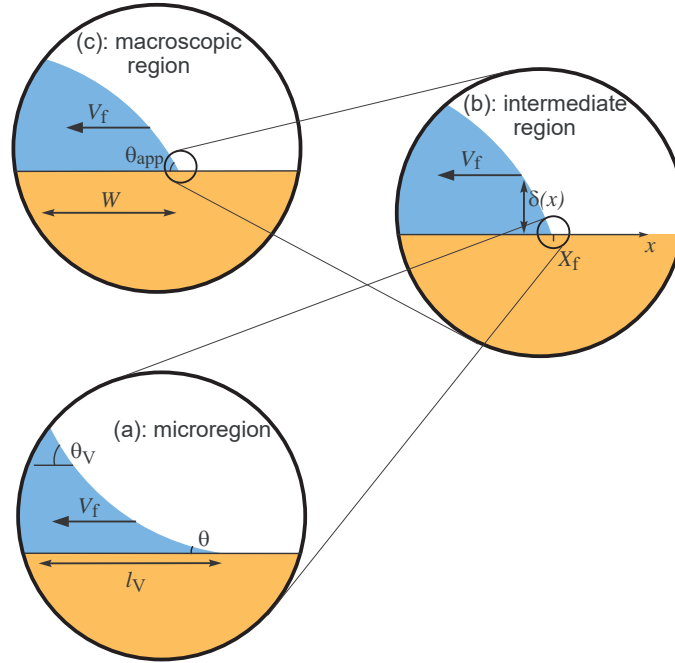


Fig. 16. Hierarchy of length scales in the moving CL problem. The microregion (a) is presented here for the partial wetting case with the microscopic contact angle θ . The shown intermediate region curvature (b) corresponds to the CL receding. The macroscopic region (c) can be compared to the CL vicinity shown e.g. in Fig. 10.

This expression is not a solution as the ultimate objective of the CL problem is to find the complete interfacial shape in the macroscopic region, in particular, the apparent contact angle θ_{app} observed at the macro-scale. Its rigorous definition is possible to give by using a fit to a known in advance macroscopic shape, i.e. that given by the balance of macro-scale forces.

Consider the phenomenon of capillary dewetting [de Gennes *et al.* (2004)]. A thin film of water on a plastic (non wetting) substrate is unstable. If one creates a hole (dry area) in it, the hole begins to grow (Fig. 17). The liquid that covered previously

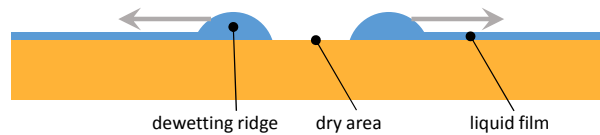


Fig. 17. Ridge formation during dewetting of the non-wetting substrate.

the dry area is not able to flow inside the film because of the strong viscous shear characteristic for the thin films. For this reason the liquid is accumulated in a ridge surrounding the dry area. The ridge shape is nearly static and is thus defined

by surface tension. Therefore, its cross-section is nearly circular. The experiment described in sec. 2.3 is very similar (see sec. 3.3.5 for the explanation why). It has been verified [Fourgeaud (2016)] that the ridge observed in these experiments (Fig. 8) is indeed circular (Fig. 18).

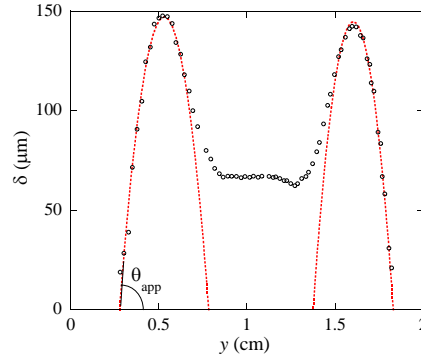


Fig. 18. Horizontal cross-section of the film shown in Fig. 8b at the height $x = 3$ cm (circles). The dotted lines are the circular arcs fits with which one finds the apparent contact angle, $\theta_{\text{app}} = 9^\circ$ in this case [Fourgeaud (2016)].

Because of geometrical singularity of CL, the microregion has a strong impact on the macroregion, in particular, on θ_{app} . To find it theoretically, one needs to resolve both the large and small scales. This is generally difficult and, numerically, the space step would need to be microscopic and, therefore, a large number of such steps would be necessary. It turns out however that such a problem can be solved separately in each of three regions. Thanks to the strong scale separation, the mathematical method of asymptotic matching can be used to assemble their solutions by performing a coupling of the conditions at the boundaries of regions. A remarkable outcome of such an approach consists in the fact that both ℓ_V and θ_V are independent of the macroregion geometry and are defined only by the microregion physics. As for the macroregion, the matching results in the expression

$$\theta_{\text{app}}^3 = \theta_V^3 - 9Ca_f \log \frac{W}{\ell_V}, \quad (29)$$

where W is the characteristic macroscopic length (Fig. 16c) that should be determined by matching of intermediate and macroscopic regions. Such a law reduces to the Hoffmann-Tanner law [Khandekar *et al.* (2010)] for the case of a spreading drop.

By using such a method, the problem of dewetting ridge has been solved by Eggers (2005); Snoeijer and Eggers (2010). They have found $W = w/e$ with $e \simeq 2.71$ and w , the ridge width. For the case of the slip length theory, they also determined that $\theta_V = \theta$ and $\ell_V = \ell_s \equiv 3l_s/(e\theta_V)$. For the case of pseudopartial wetting (wetting film at finite θ), $\ell_V = \ell_I = l_I/(2\theta_V^2)$ [de Gennes *et al.* (1990)]. One mentions that all the terms in Eq. (29) are defined so θ_{app} can be determined theoretically.

It should be noted that at capillary dewetting, the CL velocity is completely defined by the contact angle θ_V . According to the theory of Snoeijer and Eggers (2010) that agrees with numerous experiments [Snoeijer and Andreotti (2013)],

$$Ca_f = \frac{\theta_V^3}{9} \left[\log \left(a Ca_f^{1/3} \frac{w^2}{\ell_V \delta} \right) \right]^{-1}, \quad (30)$$

where $a \approx 0.15$ is constant and δ is the flat film thickness at the connection to the ridge ($\delta = \delta_0$ for the isothermal case but is smaller when evaporation is present).

Two cases should be clearly distinguished. The first is the motion of CL over the dry wall (or over the nanoscale wetting film if the wetting is complete). It is a true CL motion considered here. The second case is a motion of liquid meniscus over the Taylor bubble film. In both cases the main effect on the liquid meniscus is often seen in terms of the apparent contact angle that depends on the CL velocity. The difference between these cases lies in the different film thickness. For thick Taylor bubble films, the effect of velocity on the meniscus slope is much smaller. At receding, when the thick film is deposited, the meniscus exhibits $\theta_{app} \approx 0$. For the dry wall case, which can exist at small $Ca_f \lesssim 6 \cdot 10^{-3}$ [Snoeijer *et al.* (2006)], θ_{app} is defined by Eq. (29) and the Ca_f dependence is much stronger. For the advancing case, the difference is even more pronounced: in the case of the thick film it is difficult to reason in terms of θ_{app} because of the wavy film shape (Fig. 14b).

3.3.5. Contact line at evaporation or condensation

In this section we will consider first the micro-scale effect of the liquid flow related to the phase change for the case of the immobile CL. The effect of the phase change combined with the CL motion will be considered next. The CL velocity is defined by a macro-scale effect (like capillary dewetting, see the previous section) and can thus be considered independently of evaporation.

The phase change induces a strong liquid-vapor interface curvature in the CL region. There are two effects that cause it; the viscous pressure drop in the liquid wedge geometry and the vapor recoil pressure. We first explain the viscosity effect.

Consider a liquid wedge at the microscopic level either with a wetting (nanometric) liquid film attached to it or not (Fig. 19) and surrounded by the vapor. As we mentioned, the presence of the wetting film does not change anything. We assume an isothermal tube wall, $T_w = T_{sat} + \Delta T$, which is usually a good approximation because of its high thermal conductivity. In the first approximation, one can assume that the liquid-vapor interface temperature T^i is constant either, and equal to T_{sat} corresponding to the vapor pressure p . Since the evaporation mass flux J is given by Eq. (24), it increases strongly near the CL. This strong evaporation in the CL vicinity requires a liquid inflow to compensate the mass loss. Because of the viscous pressure drop, the liquid pressure varies along the liquid wedge (along x direction in Fig. 19). Consider two points at the interface: A and B. Point B is assumed to be closer to CL so that the liquid flows from A to B and the liquid pres-

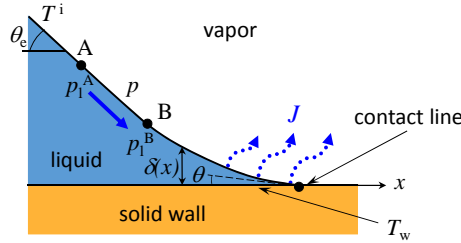


Fig. 19. Liquid wedge at evaporation in partial wetting case. The liquid flow is shown by the blue arrow.

tures in them satisfy the inequality $p_l^A > p_l^B$. The interfacial curvature K is related to the pressure via Eq. (22). Since the vapor pressure is homogeneous, the local curvatures at these points satisfy the inverse inequality: $K_l^B > K_l^A$, which means that the curvature grows near the CL, which in its turn, means that the interface is curved as outlined in Fig. 19. Namely, the interface slope far from the CL (which is the apparent contact angle observed macroscopically in such a system) turns out to be larger than its microscopic value θ . We call this apparent angle θ_e because it is caused by evaporation in the CL vicinity. This effect was discovered by Potash and Wayner (1972) for the geometry of the wedge with the attached nanometric film ($\theta = 0$ case) and studied by many other researchers. Among many others, one can mention the work of Stephan and Hammer (1994) that makes this model practical. For a long time, the disjoining pressure (necessary in this case to describe the thin film, cf. Eq. (26)) was wrongly believed to be responsible for the effect.

The second effect that can cause the interface slope increase is the vapor recoil force. When evaporation occurs, the fluid expands when changing the state from liquid to vapor. It means that on average, the evaporation-induced flow velocity in the vapor is much larger than in the liquid. To conserve the momentum at the interface, there is an additional pressure p_r exercised toward the liquid. One can show that

$$p_r = J^2 \left(\frac{1}{\rho_v} - \frac{1}{\rho} \right), \quad (31)$$

where J is the evaporation mass flux. p_r needs to be included into the interfacial pressure balance (22) that becomes

$$\sigma K = \Delta p + p_r. \quad (32)$$

Since the evaporation is strong near CL, both p_r and curvature are high there, which results in the interface bending as shown in Fig. 19 so that the apparent contact angle becomes large [Nikolayev and Beysens (1999)].

The relative contribution of these two effects varies from one situation to another. Generally, the viscosity effect is stronger than that of the vapor recoil.

To determine the length scale at which a strong interface bending occurs, one needs to consider several microscopic effects. First of all, we consider the T^i varia-

tion that occurs because of the interfacial pressure variation (Kelvin effect) and the interfacial thermal resistance [Stephan and Hammer (1994)]

$$R^i = \frac{T_{\text{sat}} \sqrt{2\pi R_v T_{\text{sat}}} (\rho - \rho_v)}{2h_{lv}^2 \rho \rho_v}$$

that appears in a linearized version of the Schrage molecular-kinetic theory [Carey (1992)]. The expression for T^i accounting for both these effects reads [Nikolayev (2010)]:

$$T^i = T_{\text{sat}} \left(1 + \frac{\Delta p}{h_{lv} \rho} \right) + R^i \frac{J}{h_{lv}}. \quad (33)$$

Each of these effects corresponds to a characteristic length [Janeček and Nikolayev (2013)]. The characteristic length for the Kelvin effect is

$$\ell_K = \frac{\sqrt{3\mu\lambda T_{\text{sat}}}}{\theta^2 \rho h_{lv}},$$

and for the interface resistance is $\ell^i = \lambda R^i$. It turns out that the largest of the characteristic lengths ℓ_I , ℓ_K , ℓ^i , and ℓ_s defines the microregion behavior (i.e. the value of ℓ_V). Typically, it is $\ell_s \simeq 50 - 100$ nm so we will use this value in what follows.

At distances from CL $X_f - x > \ell_V$ the interfacial slope induced by the phase change varies sharply and finally saturates at $x \rightarrow \infty$ at a constant value θ_e . Note that this situation is different from the flow created by the CL motion where the slope diverges logarithmically, cf. Eq. (28). Some typical dependencies of θ_e on the wall superheating are shown in Fig. 20. Note that the slope can grow from a small to very high value for a reasonable superheating.

Some analytical solutions for θ_e were obtained for the case where, among four microscale effects listed above, only the Kelvin effect is important. The asymptotic solution for small ΔT [Janeček and Nikolayev (2012)] reads

$$\theta_e = \theta + \frac{\pi \Delta T}{2\sigma \theta^2} \sqrt{\frac{3\mu\lambda}{T_{\text{sat}}}}, \quad (34)$$

so θ_e is linear in ΔT . For large ΔT , the slope becomes independent of θ [Janeček *et al.* (2013)] and varies much more weakly:

$$\theta_e \simeq \left(\frac{\sqrt{3\mu\lambda T_{\text{sat}}}}{0.3\sigma} \frac{\Delta T}{T_{\text{sat}}} \right)^{1/3}. \quad (35)$$

Note that the θ_e is the apparent contact angle observed in the presence of phase change when the CL is static.

Consider now the simultaneous phase change and CL motion. As explained above, the effect of the fluid flow caused by phase change on the interface slope manifests itself in the microregion: we saw that the characteristic scale ℓ_V of this phenomenon is extremely small. As the phase change-induced slope saturates at several ℓ_V distance from CL, the phase change can be neglected in the intermediate

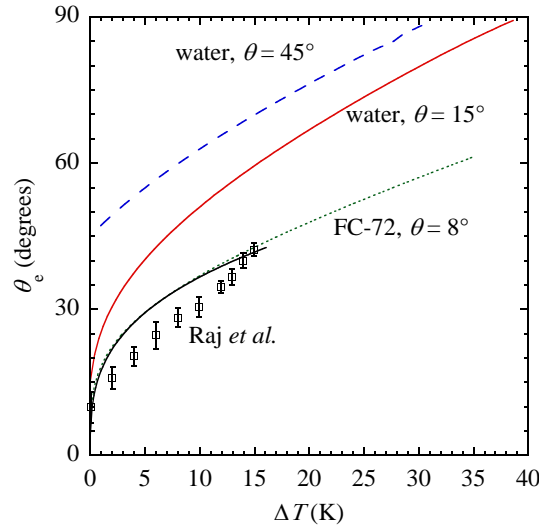
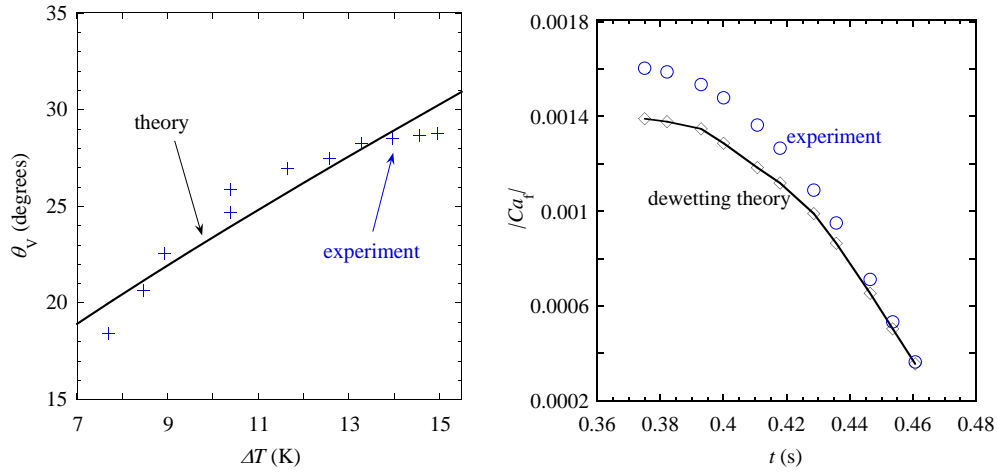


Fig. 20. Dependencies of the apparent contact angle θ_e caused by evaporation in the CL vicinity on the wall superheating ΔT [Janeček and Nikolayev (2014)] calculated for water at 10 MPa and two different θ values. Curves calculated for FC-72 at 0.04 MPa and $\theta = 8^\circ$ (dotted lines) are also shown for comparison with the theoretical results obtained for complete wetting by Raj *et al.* (2012), black solid line. Their experimental data (where $\theta = 8^\circ$) are shown with squares.

region ruled out by the flow caused by the CL motion. For this reason, these two phenomena are decoupled, and all the theory of sec. 3.3.4 can be applied to the case of CL motion where the value θ_e caused by the phase change is used for the Voinov angle θ_V . This reasoning can be corroborated by a more rigorous theory and numerical calculations [Janeček *et al.* (2013)]. For practical purposes, this means that the system behaves as if the wetting properties were controlled with the substrate superheating. These results are applicable for any phase change geometry (bubble growth in boiling, drop and film evaporation, etc.).

Let us consider the PHP liquid film to see how its length varies. Once a liquid film is deposited by the moving liquid meniscus, its CL is expected to recede because of two phenomena. First, according to the theory discussed above, the contact angle grows, and the wall dewetting occurs. Second, the liquid in the CL vicinity vaporizes; there is no flow in the film so its length decreases; in other words, CL recedes because of the evaporative mass loss. Let us discuss first the contact angle growth. Experimental data demonstrating this phenomenon have been obtained by simultaneously measuring (cf. sec. 3.3.5) the apparent contact angle θ_{app} as shown in Fig. 18, the CL velocity that defines Ca_f and the ridge width w as a function of ΔT that varied mainly because of T_{sat} variation. Then θ_V is calculated with Eq. (29). The only postulated value is that of $l_s = 20$ nm; it is used in $\ell_V = 3l_s/(e\theta_V)$. A comparison of the experimental points and the direct numerical calculation using the approach of Janeček and Nikolayev (2013) with the same l_s



(a) The Voinov angle θ_V (equivalent to θ_e because provided by evaporation) versus wall superheating ΔT . The points are obtained from experimental θ_{app} data with Eq. (29) assuming $l_s = 20$ nm. The line is a theoretical curve similar to those of Fig. 20 calculated with the approach of Janeček and Nikolayev (2013).

(b) Experimental data for the dimensionless CL receding velocity compared to the values given by Eq. (30), i.e. by the dewetting theory of Snoeijer and Eggers (2010).

Fig. 21. The dewetting theory results compared to experimental data on the PHP films (ethanol on sapphire) [Fourgeaud *et al.* (2016)].

value (Fig. 21a) shows a good agreement. The θ_V values can be high in spite of nearly zero equilibrium contact angle, cf. Fig. 9. Such high θ_V values are at the origin of the solid wall dewetting.

The apparent contact angle was also measured as a function of ΔT in an earlier experiment [Raj *et al.* (2012)] on drop evaporation with retraction, cf. Fig. 20. The discrepancy between the experimental and theoretical data can probably be attributed to the neglect of the CL velocity (i.e. of the second term in Eq. (29)).

It is important to mention that this phenomenon is not similar to a ridge [Khrustalev and Faghri (1997)] formed during static meniscus evaporation in micron-sized capillaries at high heat fluxes, because of the interfacial shear created by the vapor out-flow (that the authors called thick film phenomenon). Such an effect is expected to be negligible in the millimeter-sized capillaries, because of much larger vapor bubble cross-section and thus much lower vapor velocity.

Let us consider now the relative contribution of evaporative mass loss at the CL. Fig. 21b presents the experimental data of the CL receding velocity measured in the experiment of sec. 3.3.5 together with the result of Eq. (30), which describes only the first (dewetting) contribution [Fourgeaud *et al.* (2016)]. One can see that in this particular experiment CL recedes mainly because of the contact angle growth via dewetting; the evaporative mass loss is responsible only for 14% of the CL velocity.

For this reason, Eq. (30) is promising for development of a future liquid film model for the PHP.

We will now switch to the application of some of the above physics ideas to the PHP modeling. We will consider first the simplest PHP geometries for which the discussed above local experimental measurements can be used to validate the theoretical models.

4. Start-up and functioning of the single branch PHP

To evaluate validity of different PHP models, it is necessary to test them on simple PHP geometries, for which the models can be treated analytically to obtain general results. In addition, the local experimental data can be obtained for such geometries so a detailed comparison with the models is possible. By using these comparisons, one can adjust phenomenological parameters to use them later for simulations of the multi-branch PHP. We consider first the simplest, single-branch PHP, see Fig. 22.

The first question one can ask about the PHP is “why it oscillates?”. One can explain the functioning mechanism of the single branch PHP as follows. When the meniscus situates in the evaporator, evaporation occurs. The vapor expands and the meniscus is pushed into the condenser. The condensation occurs, and the vapor bubble contracts so the meniscus returns back into evaporator. The liquid plug inertia creates an “overshoot” of the meniscus motion which provides a phase shift between the pressure and meniscus position, which is well known to be necessary to cause self-sustained oscillations.

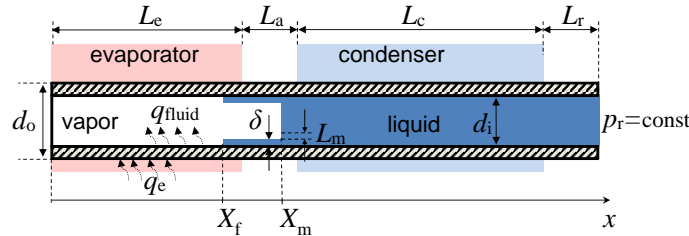


Fig. 22. The model representation of the single branch PHP and the coordinate system used in this section different from that of Fig. 5a). The lumped meniscus model is shown.

The liquid plug momentum equation stems from Eq. (13) with $p_{\text{next}} = p_r$,

$$\frac{d(V_m m_l)}{dt} = (p - p_r)S - F + G, \quad (36)$$

where

$$\dot{X}_m = V_m, \quad (37)$$

and the liquid mass should include a part of the liquid in the reservoir that is brought to motion during oscillation.

We consider first the simplest version of the model where the conduction via the PHP tube is neglected and the temperatures of the inner tube walls are imposed to be constant and equal to T_c and T_e in condenser and evaporator, respectively. The heat exchange with the tube is assumed to be absent in the adiabatic section. This is an assumption applied in many models [Shafii *et al.* (2001); Dobson (2004); Das *et al.* (2010)]. In this case the heat exchange inside the liquid does not impact the plug dynamics and can be solved *a posteriori* to evaluate the global heat exchange. In the next stage, we introduce the heat conduction through the tube walls and caused by it smooth wall temperature variation, see sec. 4.2.2 below.

When experimentalists consider the PHP start-up, they speak usually of what happens after the power switching-on. Two situations are then possible: either PHP begins to oscillate or it comes to some stationary non-oscillating state of dynamic equilibrium (that we will call simply equilibrium for the sake of brevity). One does not need to consider the switching-on procedure when approaching the start-up problem theoretically. One needs to find instead an equilibrium state and see if it is stable or unstable with respect to a small fluctuation. The stable state corresponds to that found experimentally and means the absence of oscillation while an unstable oscillatory mode corresponds to the oscillation start-up. We describe now two models most commonly used for the PHP simulation and analyze the stability of the single-branch PHP described within each of them.

4.1. Superheated vapor model

Many theoretical works (see e.g. [Dobson (2004); Holley and Faghri (2005); Yuan *et al.* (2010); Shao and Zhang (2011); Cheng and Ma (2011); Mameli *et al.* (2012); Ma (2015)]) are based on the original model of Shafii *et al.* (2001). Several simplification hypotheses have been adopted in it. We list below the most important of them.

- (1) The model is one-dimensional.
- (2) The liquid films are assumed to completely cover the internal tube walls inside the vapor bubbles.
- (3) The films are of the constant thickness δ .
- (4) The temperature of the liquid-vapor interface of the films T^i is equal to the vapor temperature T .

The last hypothesis and its validity has been already discussed in the section 3.2.

The film mass is $m_f = \rho \delta S_f^i$ where S_f^i is the film interface area. For the circular tube,

$$S_f^i = \pi(d_i - \delta)L_v \simeq \pi d_i L_v, \quad (38)$$

where L_v is the vapor bubble length. The film mass exchange rate due to evapora-

tion/condensation is

$$\dot{m}_f = \int_{(S_f^i)} J dS. \quad (39)$$

The evaporation mass flux J is given by Eq. (24) where the interface temperature T^i is replaced by the vapor temperature T according to the hypothesis (4) above. For example, for the case of a bubble of the length L_v in a circular tube of constant temperature $T_{w,k}$ ($k = e$ with $T_{w,e} \equiv T_e$ in evaporator and $k = c$ in the condenser) this expression reduces to [Dobson (2004)]

$$\dot{m}_{f,k} = \frac{U_f}{h_{lv}} \pi d_i L_{v,k} (T_{w,k} - T), \quad (40)$$

with U_f , the film heat transfer coefficient. For simplicity, we write all the formulas within an additional hypothesis (that was not applied in the above research articles) that the film thickness is the same in both the condenser and the evaporator, so are the heat transfer coefficients. Under $L_{v,k}$ we mean a portion of the bubble belonging to the section k . Accordingly, the heat taken from the wall is

$$\dot{Q}_{v,k} = h_{lv} \dot{m}_{f,k} = U_f \pi d_i L_{v,k} (T_{w,k} - T). \quad (41)$$

The fluid mass conservation inside the PHP (one would normally need to add the condensed mass to the liquid plug and vice versa, subtract the evaporated mass) is usually ignored in this model.

Note that Eq. (41) can be seen as describing the heat exchange between the vapor and completely dry (instead of completely film-covered) walls and no phase change, cf. Eq. (18). For this reason, the above model was called by Das *et al.* (2010) “superheated vapor model” as opposed to the introduced by them “film evaporation-condensation (FEC) model” presented in sec. 4.2 below. Consequently, there are two possible versions of the superheated vapor model. We begin the discussion with the first (“mass-spring” or “no films at all”) formulation [Das *et al.* (2010)]. It corresponds to the vapor energy balance written for the fixed vapor mass m so (19) reduces to $mc_{vv}\dot{T} = \dot{Q}_v - p\dot{\Omega}$. Within this formulation, U_f has a meaning of the vapor-wall heat exchange, i.e. U_v . By using $\dot{Q}_v = \dot{Q}_{v,e} + \dot{Q}_{v,c}$ and Eq. (41), one obtains

$$mc_{vv}\dot{T} = U_f \pi d_i [L_{v,e}(T_e - T) + L_{v,c}(T_c - T)] - pSV_m. \quad (42)$$

The lengths of the vapor in contact with the evaporator and the condenser are defined by the expressions

$$L_{v,e} = \begin{cases} X_m, & X_m \leq L_e \\ L_e, & \text{otherwise,} \end{cases} \quad (43)$$

$$L_{v,c} = \begin{cases} 0, & X_m < L_e + L_a, \\ X_m - (L_e + L_a), & L_e + L_a \leq X_m < L_e + L_a + L_c, \\ L_c, & \text{otherwise.} \end{cases} \quad (44)$$

The system is governed by the set of differential Eqs. (36,37,42) and the EOS (17). The viscous friction and gravity are neglected for simplicity. Such a description corresponds to the superheated vapor (ideal gas) subjected to heat transfer with no phase change.

The start-up of oscillations in such a model can be studied analytically [Das *et al.* (2010)] via the conventional linear stability analysis. First one finds equilibrium states (denoted by the over bar hereafter) by zeroing the time derivatives. Then a small perturbation of such a state is introduced. One linearizes the set of equations with respect to the perturbations and finds a condition for their growth (i.e. when the equilibrium is unstable). For such a model, the equilibrium meniscus position can exist at any place, either in evaporator, or adiabatic, or condenser sections. The equilibrium meniscus positions in evaporator and adiabatic sections are stable for any system parameters. This is a nonphysical result. Indeed, when an experimentalist wants to start-up a single-branch PHP, the meniscus is brought precisely to the evaporator or adiabatic sections [Recklin *et al.* (2015); Fourgeaud *et al.* (2017)].

For equilibrium meniscus positions located in the condenser (i.e. for $L_e + L_a \leq \bar{X}_m < L_e + L_a + L_c$), the instability occurs when [Das *et al.* (2010)]

$$\bar{T} - T_c > (\gamma - 1)\bar{T} \left(1 - \frac{L_a}{\bar{X}_m} \right), \quad (45)$$

where the equilibrium vapor temperature \bar{T} is determined by the following expression obtained by cancelling the derivatives in Eq. (42),

$$\bar{T} = \frac{L_e T_e + (\bar{X}_m - L_e - L_a) T_c}{\bar{X}_m - L_a} \quad (46)$$

Since \bar{T} grows with T_e , the condition (45) is roughly equivalent to the statement that the difference $T_e - T_c$ must exceed a threshold. A numerical solution of Eqs. (36, 37, 42) indeed exhibits oscillations that develop under condition (45). The model however shows a nonphysical behavior. At many combinations of parameters, the oscillations occur while the meniscus remains inside the condenser during the whole oscillation cycle [Das *et al.* (2010)], so no evaporation is possible. Generally, the amplitude of oscillations is quite small with respect to the evaporator length.

Let us now consider the oscillation start-up within a formulation that corresponds to the liquid films *covering entirely* the tube inside the vapor bubbles, i.e. $L_d = 0$. This is the formulation used originally by Shafii *et al.* (2001). In this case the vapor mass varies due to the film evaporation-condensation. The phase change rate is introduced via Eq. (40). Like in the approach of Shafii *et al.* (2001), the time variation of vapor mass is

$$\dot{m} = \frac{U_f}{h_{lv}} \pi d_i [L_{v,e}(T_e - T) + L_{v,c}(T_c - T)]. \quad (47)$$

The vapor energy balance (19) should now be used (with $\dot{Q}_v = 0$ according to Eq. (18) and the hypothesis (4). Such an equation can be solved analytically as

discussed in sec. 3.2.2 and leads to Eq. (21). Since the pressure is homogeneous at equilibrium, $\bar{p} = p_r$ and the coefficient in Eq. (21) can be determined explicitly:

$$p = p_r \left(\frac{T}{\bar{T}} \right)^{\frac{\gamma}{\gamma-1}}. \quad (48)$$

By using EOS (17), one can express T through m and X_m :

$$T = \bar{T} \left(\frac{\bar{T} R_v m}{p_r S x_m} \right)^{\gamma-1}. \quad (49)$$

With the substitution of two latter equations, Eqs. (36, 37, 47) form a closed system, the stability of which can now be analyzed. It is interesting that the results are exactly the same as for the set of Eqs. (36, 37, 42). Moreover, by expressing m as a function of T and X_m with Eq. (49) and taking its derivative, one obtains exactly Eq. (42) with U_f replaced by $U_f R_v T / h_{lv}$. In other words, the start-up analysis shows the equivalence of both formulations of the superheated vapor model. However, as shown above, the formulation with no films behaves in a nonphysical way. To conclude this part, the model formulated initially by Shafii *et al.* (2001) and used at present by many research groups is not fully adequate, at least for the single branch PHP, and for this reason may hardly be considered as reliable for advanced multi-branch PHP modeling. One has thus to develop another model like the one discussed in the next section.

4.2. Film evaporation-condensation (FEC) model

To begin with, we present here the model for the single-branch PHP; the multi-branch version will be presented later on, in sec. 6.

The FEC model is an extension of the superheated vapor model, where the hypotheses (2) and (4) are abandoned. In particular, the vapor temperature T is not assumed any more to be equal to T_{sat} (which is generally inconsistent, cf. sec. 3.2). The liquid-vapor interface temperature T^i is equal to T_{sat} in Eq. (24) instead of T in the superheated vapor model.

The hypotheses (2) is now abandoned and a dry area at the internal tube walls is allowed. The actual meniscus shape (Fig. 10) is approximated with the lumped representation (Fig. 22) introduced initially by Dobson (2004). The film length is assumed to vary because of two factors, the phase change and the meniscus motion over the film. During the meniscus advancing, the film length reduces and vice-versa. This can be described by the CL dynamics equation [Nikolayev (2016)]

$$V_f = \begin{cases} V_m & \text{if } X_f \geq X_m, V_m < 0, \\ \dot{m}_{f,e} / (\rho \pi d_i \delta) & \text{otherwise,} \end{cases} \quad (50)$$

where $V_f = \dot{X}_f$ is the velocity of the film edge (i.e. of CL position X_f). The first line of Eq. (50) is introduced to make X_f coincide with the meniscus position X_m during the meniscus advancing over the dry area when the film length is zero. In

all other cases, the film edge recedes because of the film evaporation contribution defined by the evaporation part $\dot{m}_{f,e}$ of the total film mass change rate \dot{m}_f . The film can cover at the same time parts of both evaporator and condenser. The film length is then controlled only by the evaporator-located part of the film. This is necessary to avoid a nonphysical film extension. Imagine a situation where X_f situates in evaporator but X_m is so deep in the condenser that the film condensation in the condenser overcomes the film evaporation in the evaporator. If one used the full film contribution \dot{m}_f in Eq. (50), V_f would be negative. This should be forbidden because the liquid flow in the film is very slow so the liquid mass is not transferred instantly between condenser and evaporator-located parts of the film. The other part of the mass $\dot{m}_{f,c}$ (condensed onto the film) is added to the liquid plug to conserve the total fluid mass.

In the following, we consider separately two FEC model statements, first for the constant temperatures of the internal tube wall in the evaporator and condenser sections, and next for the smooth temperature variation along the tube due to its heat conduction.

4.2.1. FEC model for imposed temperatures in evaporator and condenser

Imagine that the tube temperatures are T_e and T_c in evaporator and condenser, respectively, and both these values are constant due to high heat capacity of the solid. Instead of Eq. (40), one obtains the following expression for the film phase change rate [Das *et al.* (2010)] $\dot{m}_f = \dot{m}_{f,e} + \dot{m}_{f,c}$ where

$$\dot{m}_{f,k} = \frac{U_f}{h_{lv}} \pi d_i L_{f,k} (T_{w,k} - T_{sat}(p)), \quad (51)$$

with $U_f \sim \lambda/\delta$. A coefficient of proportionality of the order 1 (the film form factor) is introduced to account for the film slope that exists in reality. $L_{f,k}$ is the film length belonging to the section k , which is not necessarily equal to $L_{v,k}$:

$$L_{f,c} = \begin{cases} 0, & \text{if } X_m \leq L_e, \\ X_m - L_e, & \text{if } L_e < X_m \leq L_e + L_c, \\ L_c, & \text{otherwise.} \end{cases} \quad (52)$$

$$L_{f,e} = \begin{cases} X_m - X_f, & \text{if } X_f < X_m < L_e, \\ 0, & \text{if } X_m \leq X_f, \\ L_e - X_f, & \text{if } X_m \geq L_e. \end{cases} \quad (53)$$

An approach employing Eq. (51) with $L_{f,k} = L_{v,k}$, i.e. with continuous films, has been taken by Dilawar and Pattamatta (2013). Note that the expression for evaporation rate proportional to $[p_{sat}(T_{w,k}) - p]$ used by Senjaya and Inoue (2013b) is quite similar to Eq. (51).

The total vapor change rate

$$\dot{m} = \dot{m}_f + \dot{m}_m, \quad (54)$$

includes the meniscus contribution that exists even in the absence of the film. More precisely, it corresponds to the contribution of the CL vicinity (cf. sec. 3.3.5) of the size L_m (Fig. 22) over which the heat exchange coefficient is denoted U_m ,

$$\dot{m}_m = \frac{U_m L_m \pi d_i}{h_{lv}} [T_w(X_m) - T_{sat}]. \quad (55)$$

The full mathematical problem includes now five differential equations for the variables V_m, T, m, X_m, X_f (instead of three in the superheated vapor model). First two are the mechanical momentum Eq. (36) and vapor energy Eq. (19). One cannot solve the latter directly any more (nor use Eq. (21) instead) because dry areas are allowed and one needs to account for \dot{Q}_v given by Eq. (18). The importance of the direct vapor-solid heat exchange \dot{Q}_v will be discussed below in sec. 4.4. Other three differential equations of the model are Eqs. (37, 50, 54). The EOS (17) closes the problem.

4.2.2. Introduction of the thermal fluid-solid coupling

In a general case of the spatial variation of the tube wall temperature, instead of (51), the film mass exchange reads

$$\dot{m}_f = \frac{U_f \pi d_i}{h_{lv}} \int_{X_f}^{X_m} [T_w(x) - T_{sat}] dx. \quad (56)$$

To define the evaporation contribution needed for the FEC model, one needs to introduce a notion of the effective evaporator as a time varying area over which $T_w > T_{sat}$. In the single-branch PHP the $T_w(x)$ variation is monotonous (cf. Fig. 26 below); the effective evaporator length X_e can be determined from the equation

$$T_w(X_e) = T_{sat}. \quad (57)$$

In the case of the fixed evaporator temperature [Das *et al.* (2010); Nikolayev (2011b, 2013)], the effective evaporator is fixed and coincides with the actual evaporator, $X_e = L_e$. $\dot{m}_{f,e}$ can now be defined as

$$\dot{m}_{f,e} = \frac{U_f \pi d_i}{h_{lv}} \int_{X_f}^{X_e} [T_w(x) - T_{sat}] dx. \quad (58)$$

Such a definition always provides the liquid films covering the tube walls in the effective condenser (a section where $T_w(x) < T_{sat}$), which corresponds to the condenser and adiabatic sections for imposed T_e and T_c case.

The temperature distribution along the internal tube wall is described by the equation

$$\frac{\partial T_w}{\partial t} = D_w \frac{\partial^2 T_w}{\partial x^2} + \frac{j_w}{\rho_w c_w} \quad (59)$$

first introduced by Holley and Faghri (2005). It is solved within the evaporator and adiabatic section. The temperature is assumed to be constant $T_w(x) = T_c$ within

the condenser. The effective volume heat source is

$$j_w = \frac{\pi}{S_w} \begin{cases} q_e d_o - q_{\text{fluid}} d_i & \text{if } 0 < x \leq L_e, \\ -d_i q_{\text{fluid}} & \text{if } L_e < x \leq L_e + L_a, \end{cases} \quad (60)$$

where $S_w = \pi(d_o^2 - d_i^2)/4$ is the tube material cross-section area. In the problems with smooth temperature distribution we assume that the heat flux q_e applied to the evaporator is distributed uniformly and is thus constant,

$$q_e = \frac{P_e}{\pi d_o L_e}. \quad (61)$$

The heat flux $q_{\text{fluid}} = U_{\text{fluid}}(x)(T_w(x) - T_{\text{fluid}}(x))$ is transferred from the internal tube wall to the fluid. It can vary in time and space. The definitions of T_{fluid} and U_{fluid} are

$$T_{\text{fluid}}(x) = \begin{cases} T & \text{if } x \in \text{gas bubble}, \\ T_{\text{sat}} & \text{if } x \in \text{liquid film}, \\ T_l(x) & \text{if } x \in \text{bulk liquid}, \end{cases} \quad \text{and} \quad U_{\text{fluid}}(x) = \begin{cases} U_v & \text{if } x \in \text{gas bubble}, \\ U_f & \text{if } x \in \text{liquid film}, \\ U_l & \text{if } x \in \text{bulk liquid}, \end{cases} \quad (62)$$

where the fluid regions are those in contact with the wall at the position x and $U_l = Nu_l \lambda_l / d_i$. One can see that, unlike the imposed wall temperature case, the liquid temperature influences the meniscus dynamics through the wall heat conduction by impacting the wall temperature in the vapor region.

The choice of the boundary conditions for the thermal diffusion problem is of importance. It is often assumed that the condenser is efficient enough to impose a constant temperature T_c at its boundary,

$$T_w(x = L_e + L_a) = T_c. \quad (63)$$

Sometimes the condenser cooling efficiency cannot be assumed infinite so its temperature cannot be imposed. One introduces in this case a (high) heat transfer coefficient U_∞ toward the environment (e.g. via the external air cooler) with a temperature T_∞ . In this case Eq. (59) is solved over all the tube length and one defines

$$j_w = \frac{\pi}{S_w} \{d_o U_\infty [T_\infty - T_w(x)] - q_{\text{fluid}} d_i\} \quad (64)$$

in the condenser section.

The adiabatic condition is usually a good approximation at the sealed end of the tube,

$$\left. \frac{\partial T_w}{\partial x} \right|_{x=0} = 0. \quad (65)$$

The above description of evaporator is often inexact because of the thermal interaction with the heat spreaders used commonly to reduce the temperature fluctuations that otherwise might be strong. On one hand, a thermal spreader provides

a thermal inertia that smoothes the temporal fluctuations. On the other hand, a spreader thermally shunts the tube so the spatial fluctuations are also reduced. Generally, to describe a spreader, one needs to write a separate heat diffusion equation for it and introduce its thermal interaction with the tube. An example of such a model is given by Gully *et al.* (2014) and the steady oscillations simulated within such a model are shown in Fig. 4b.

For a multi-branch PHP, a spreader introduces a very important feature of thermal interaction between the PHP branches which postpones the local PHP dryout.

4.3. Liquid heat transfer

Within the Lagrangian formulation, in the reference of the center of mass of the liquid plug, the heat exchange in the liquid is usually assumed to obey the thermal diffusion equation

$$\frac{\partial T_1}{\partial t} = D_1 \frac{\partial^2 T_1}{\partial x'^2} + \frac{\pi d U_1}{\rho c_1 S} (T_w(x') - T_1(x')). \quad (66)$$

Its delicate part is a determination of $T_w(x')$ corresponding to $x' = x - X_m(t)$ defined in the moving plug reference.

The saturation temperature at the liquid meniscus

$$T_1(x' = 0) = T_{\text{sat}}(p). \quad (67)$$

provides both boundary conditions for the plugs of a closed multi-branch PHP. For a PHP open to a reservoir one needs another boundary condition. The thickness of thermal boundary layer formed near the liquid meniscus is of the order $\sqrt{D_1/\omega_0}$, where ω_0 is the frequency of meniscus oscillations. It is assumed to be much smaller than the liquid penetration length into the adiabatic section. We will see below that such an assumption is often justified for the single-branch PHP. This means that in case of the imposed wall temperature T_c in the condenser, the liquid temperature inside it is also equal to T_c and

$$T_1(x' = L_e + L_a - X_m) = T_c. \quad (68)$$

With these assumptions, the integration interval may be reduced. E.g. for the single branch PHP it is limited to the intervals $0 < x < L_e + L_a$ and to $0 < x' < L_e + L_a - X_m$ for Eqs. (59) and (66), respectively.

One notes that in the case of imposed temperatures both in the condenser and evaporator sections, the liquid temperature impacts neither the vapor bubble state nor the overall PHP dynamics. The dynamic problem includes only five ordinary differential equations (in case of the FEC model). To determine the global PHP heat transfer discussed in sec. 5.1, Eq. (66) is solved *a posteriori*, after the plug dynamics calculations. When the thermal conduction via the PHP tube is introduced, five ordinary differential equations need to be solved together with the partial differential

equations (59, 66) at each time step. Evidently, this makes the problem much more complicated.

4.4. FEC model: steady regime of single branch PHP

The steady regime can be defined as a regime where the system state averaged over the oscillation period remains constant in time. In this regime, the frequency of

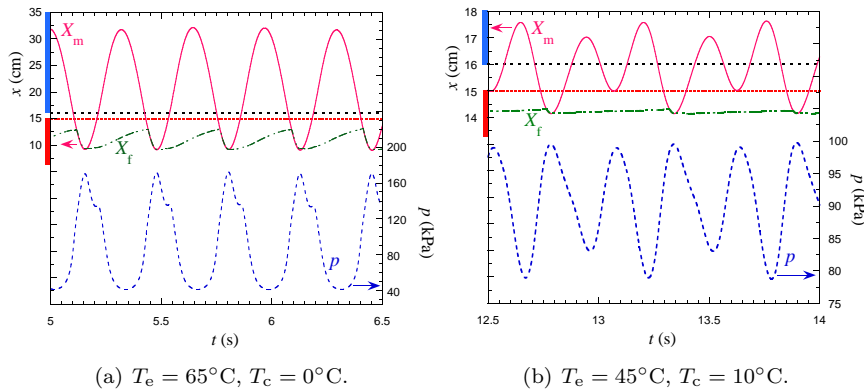


Fig. 23. FEC model simulation results with imposed T_e and T_c for the single branch PHP for n-pentane as the working fluid at $p_r = 90.6$ kPa [Das *et al.* (2010)]. The lower and upper horizontal lines correspond to the ends of the evaporator ($L_e = 15$ cm) and adiabatic sections ($L_e + L_a = 16$ cm), respectively. The evaporator and the condenser are shown with red and blue bars, respectively.

oscillations in the single branch PHP is characterized by the eigenfrequency of the inviscid liquid column [Das *et al.* (2010)] of the average length \bar{L}_1 ,

$$\omega_0 = \sqrt{\frac{\gamma p_r}{\rho \bar{L}_1 \bar{L}_v}}, \quad (69)$$

(where $\bar{L}_v \equiv \bar{X}_m$ is the averaged over oscillation vapor bubble length) and depends only weakly on the phase change intensity. When the PHP tube is vertical, the gravity term appears as mentioned in sec. 3.1.2:

$$\omega_0 = \sqrt{\frac{\gamma p_r}{\rho \bar{L}_1 \bar{L}_v} + \frac{g}{\bar{L}_1}}. \quad (70)$$

As for the simulated PHP dynamics (Fig. 23), one clearly observes a strong effect of the vapor compression: the maximal vapor pressure is attained when X_m is (nearly) the smallest, i.e. for the leftmost in Fig. 22 position of the meniscus.

Two oscillation regimes has been predicted. In the first regime, the meniscus oscillations are quasi-sinusoidal (Fig. 23a). The same regime was observed by Gully *et al.* (2014) (Fig. 4a). In the second regime, the amplitudes of two consecutive meniscus strokes strongly differ so the meniscus penetrates into evaporator each

second stroke and the period of oscillation is doubled (Fig. 23b). These regimes were clearly observed experimentally [Rao *et al.* (2013, 2015)]. The quasi-sinusoidal regime (Fig. 23a) appears when the film phase exchange is strong so the film length (corresponding to the evaporated film mass in FEC model) changes considerably over an oscillation period, the oscillation amplitude is large and the liquid plug inertia is strong. The period doubling (Fig. 23b) appears when the film mass exchange is not strong and the system needs a larger time to accumulate large enough evaporated mass. As the period of oscillations is imposed, the system uses several oscillation periods for this. This regime has been discussed in detail by Rao *et al.* (2013, 2015, 2017). They have shown experimentally that a phase shift can exist between X_m and p : p maximum occurs when the vapor volume increases from its minimum (Fig. 24), i.e. during receding of the liquid meniscus. This shift is explained by the contribution of film evaporation (i.e. vapor mass increase) that causes the vapor pressure increase according to Eq. (17). Indeed, when the liquid meniscus recedes, the film area in evaporator grows and evaporation increases.

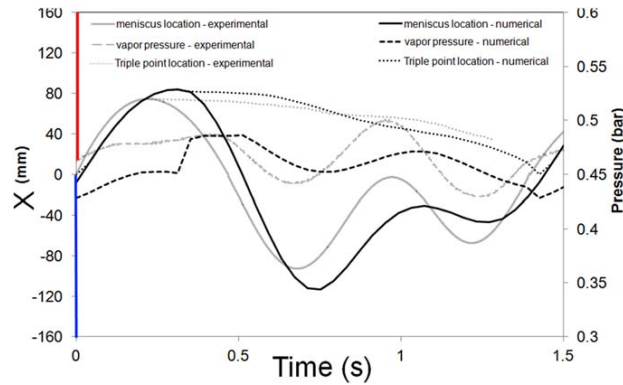


Fig. 24. Comparison of experimental data and simulation (performed with the extended FEC model, cf. sec. 4.7) for meniscus movement, triple line movement and vapor pressure for FC72 with $T_e = 37.5^\circ\text{C}$, $T_c = 16^\circ\text{C}$, $p_r = 50\text{ kPa}$ for one period of oscillations [Rao *et al.* (2017)]. The evolution of X_m , X_f and p is shown with red, green, and blue colors, respectively. The theoretical and experimental data are shown with solid and dotted curves, respectively. The evaporator and the condenser are shown with the red and blue bars, respectively.

4.5. Start-up of oscillations in single branch PHP with imposed temperatures in evaporator and condenser: FEC model

It is interesting to compare the oscillation threshold result with the superheated vapor model. It is evident that if $L_a \neq 0$, any meniscus position situating inside the adiabatic section is the equilibrium position so a small deviation from it would not lead to the start-up. For this reason, we consider the simplest case $L_a = 0$. It is equivalent to a replacement of the actual smooth temperature variation along

the tube by a stepwise variation. One easily finds that the only stationary state is possible when the meniscus situates at the boundary between the evaporator and the condenser.

It is difficult to define the start-up conditions in the general case because the parameters are too many and the diagram would be multidimensional. It is however possible to obtain it in the approximation of small temperature difference $T_e - T_c$, more specifically, in the approximation of the small dimensionless quantities

$$\alpha_c = \frac{U_f[T_{\text{sat}}(p_r) - T_c]}{\omega_0 \rho h_{lv} \delta}, \quad (71)$$

$$\alpha_e = \frac{U_f[T_e - T_{\text{sat}}(p_r)]}{\omega_0 \rho h_{lv} \delta}, \quad (72)$$

where ω_0 is given by Eq. (69). The parameters α_c and α_e characterize the film condensation in the condenser and film evaporation in the evaporator, respectively. The parameter

$$\Gamma = \frac{U_v(\gamma - 1)}{\omega_0 c_{vv} \rho \delta} \quad (73)$$

characterizes the heat exchange of the tube with the vapor. The threshold criterion

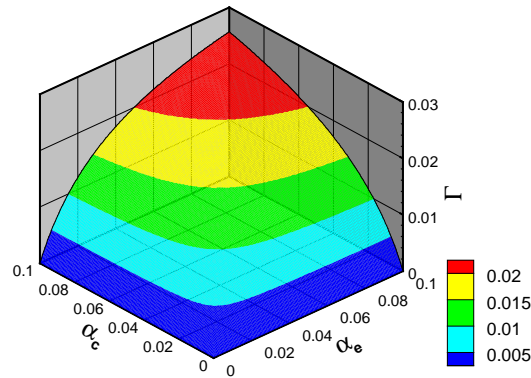


Fig. 25. Instability boundary for the single branch PHP with imposed temperatures in evaporator and condenser in the parameter space $(\alpha_c, \alpha_e, \Gamma)$ [Nikolayev (2013)]. The boundary is presented as a surface which is the dependence of Γ on α_c and α_e . The oscillations can develop for the points below the surface.

may be expressed as $\Gamma = f(\alpha_c, \alpha_e)$. The surface corresponding to this function is shown in Fig. 25. The system is unstable (i.e. the PHP starts up) for the parameters that correspond to the points below the surface (i.e. for $\Gamma < f(\alpha_c, \alpha_e)$) and stable for the points above the surface.

Several general conclusions can be made from this figure. First, both condensation and evaporation are necessary for oscillations, which corresponds to the inequality

$$T_c < T_{\text{sat}}(p_r) < T_e. \quad (74)$$

Indeed, if either α_c or α_e are zero, no instability is possible. The increase of α_c or α_e favors the instability. If the system is characterized by a point located above the surface in Fig. 25 (i.e. in the stable region), an appropriate increase of α_c and α_e (achieved e.g. by increasing the temperature difference $T_e - T_c$) brings the system to the instability. This qualitatively agrees with experiments. The threshold value of the above temperature difference is one of the few well established features of the PHP start-up [Zhang and Faghri (2008)].

Another consequence of Fig. 25 is that the heat exchange of the dry evaporator walls with the vapor (characterized by Γ) hinders the oscillations and can be thus considered as a channel of energy dissipation. Indeed, an increase of Γ may bring the system above the surface in Fig. 25, where the system is stable. This feature can be easily understood. Since the heat exchange between the dry evaporator walls and the gas does not contribute to the evaporation/condensation mass exchange (which is the moving force of oscillations), the corresponding energy is lost, which means that Γ characterizes the energy dissipation. This means that, in general, the fluids with low vapor heat conductivity are advantageous for the PHP.

Since the film thickness is an independent parameter of this model (in reality, it is defined by the meniscus velocity), one can consider the dependence of the threshold on it. On one hand, an increase of δ leads to the decrease of α_c and α_e (cf. Eqs. (71, 72) and thus hinders the instability. On the other, it leads to the decrease of Γ (cf. Eq. 73)), which favors the instability. This means that in general there is a range of δ , for which the oscillations develop. Beyond this range the system is stable.

4.6. *Start-up of oscillations in single branch PHP with smooth temperature distribution: FEC model*

The account of the thermal interaction of the fluid with the tube complicates strongly the problem because one needs to solve much more complex equations and the number of parameters is much larger. However the account of thermal interaction is of importance because it changes substantially the system dynamics and start-up criteria as will be shown below. This problem in a general case $L_a \neq 0$ was considered by Nikolayev (2016). Unlike the imposed temperatures case, there is a single equilibrium state (i.e. temperature distribution and meniscus position, see Fig. 25) for each set of parameters, in particular evaporator power and condenser temperature. It is evident that the equilibrium meniscus position \bar{X}_m coincides with the end of the effective evaporator \bar{X}_e (any deviation from it would case the mass exchange). By definition of the effective evaporator length, the wall temperature at this point coincides with $\bar{T}_{\text{sat}} > T_c$ which is apparent in Fig. 26. This means that \bar{X}_m cannot belong to the condenser. In this particular case \bar{X}_m situates in the adiabatic section.

It turns out that the relevant parameter for the start-up criterion is the gradient

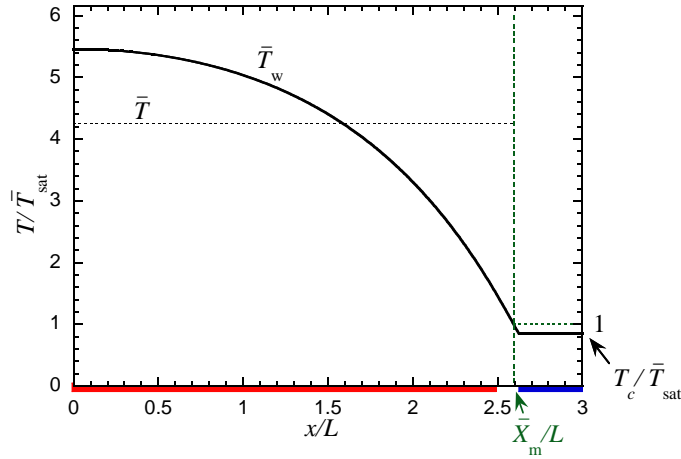


Fig. 26. An example [Nikolayev (2016)] of equilibrium temperature distribution $\bar{T}_w(x)$ along the PHP tube (solid curve). The corresponding vapor temperature \bar{T} is shown inside the vapor with a dotted line. The coordinate is expressed in terms of the characteristic length $L = \sqrt{S_w k_w / (\pi d_i U_v)}$ of the heat exchange in the dry tube while the temperatures are made dimensionless with $\bar{T}_{\text{sat}} = T_{\text{sat}}(p_r)$. The locations of evaporator and condenser are shown with the red and blue bars, respectively. The boundary between the effective evaporator and condenser (i.e. equilibrium meniscus position) is in the adiabatic section for this particular case.

of \bar{T}_w at $x = \bar{X}_m$. When $\bar{X}_m > L_e$, this quantity is defined by the evaporator power,

$$-\left. \frac{d\bar{T}_w}{dx} \right|_{x=\bar{X}_m} = \frac{P_e}{S_w k_w}. \quad (75)$$

Such a formula may seem counter-intuitive because one may imagine that the temperature gradient is equal to the difference between the condenser and evaporator temperatures divided by the sum of the evaporator and adiabatic lengths. This expression is easier to understand if one recalls that this temperature difference appears due to the power injection into evaporator. For the case $\bar{X}_m < L_e$, the r.h.s. of Eq. (75) should be multiplied by \bar{X}_m/L_e .

An analytical instability criterion [Nikolayev (2016)] can be obtained within two approximations. First, it is the approximation of massive tube so at small deviations from equilibrium the tube thermal response is slow and the temperature distribution in it is the equilibrium distribution (Fig. 26). Second, it is the same kind of averaging approximation as for the imposed constant temperatures case that corresponds to small evaporator power. Within these approximations, one obtains the start-up threshold [Nikolayev (2016)]

$$-\left. \frac{d\bar{T}_w}{dx} \right|_{x=\bar{X}_m}^{\text{start-up}} = \left(\frac{\bar{X}_m}{\gamma p_r} \frac{d\bar{p}}{dT} \Big|_{\text{sat}} \right)^{-1} + \frac{U_v h_{lv}}{U_m L_m R_v} \frac{(\gamma - 1)^2}{\gamma} + \frac{8\nu p_r h_{lv}}{d_i \bar{T} U_m L_m R_v}. \quad (76)$$

One can see that the threshold is defined by three additive terms. The first term presents the inverse efficiency of phase change expressed in terms of the slope

of saturation curve (cf. Fig. 3). This means that the high slope of saturation curve favors the oscillation start-up. This is generally found experimentally, see Chapter 1. There are many other PHP parameters (like e.g. T_c) that influence the threshold through this term because \bar{X}_m depends on them (this concerns also the quantity \bar{T} in the third term). The two other terms correspond to different dissipation channels that need to be overcome to create self-sustained oscillations. The second term is related to the energy loss (in a sense that it is lost for creation of oscillations) appearing because of the tube-vapor heat exchange as already discussed in sec. 4.5. The last term is the contribution of viscous dissipation. Usually this term is expected to be smaller than the previous; however its contribution is inversely proportional to the tube diameter and may become crucial for thin capillaries.

Important feature of the start-up threshold is its independence of the film thickness, which suggests that the criterion (76) is independent of the particular film model. Instead, this formula shows the crucial role of the mass exchange at the meniscus for the oscillation start-up. One recalls that the meniscus mass exchange is provided by the meniscus part closest to the wall. In the absence of the film, this is the CL vicinity. The meniscus mass exchange is described by the group $U_m L_m / h_{lv}$. Once it is put to zero, the threshold becomes infinite so the oscillation start-up is impossible. This feature is completely different from the imposed temperatures case where the PHP can start oscillations due to the film exchange alone. One can see that the account of the tube heat conduction is very important for the correct understanding of the PHP start-up.

A comparison of Eqs. (75, 76) shows a strong dependence of the threshold evaporator power on the tube parameters: it is (roughly) proportional to the product $S_w k_w$. This occurs because a larger heat conductivity requires a larger power to produce the same temperature gradient. One may guess that this result will apply to the multi-branch PHP.

The threshold depends only weakly on condenser temperature or adiabatic section length. Such a situation is characteristic to an open PHP (that connected to a reservoir with the imposed pressure) for which the relevant parameter is the saturation temperature corresponding to the reservoir pressure rather than the condenser temperature. The role of T_c in the open PHP is to bring meniscus close to the condenser, i.e. to increase the bubble length \bar{X}_m thus lowering the oscillation threshold.

To conclude this section, the PHP starts oscillating when the evaporator power exceeds energy dissipation and the phase change is efficient enough. Two causes of energy dissipation has been evidenced: the heat losses appearing because of vapor-tube heat exchange and liquid viscous dissipation. The FEC model gives the start-up threshold that can be easily interpreted and, conceptually, is more realistic than the threshold given by the superheated vapor model.

4.7. Single branch PHP description: beyond FEC model

The film evaporation-condensation model is a “minimal” solution but not necessarily the best from the physical point of view, because implicitly assumes an instant end-to-end hydrodynamic flow along the film, which is nonphysical. Indeed, within such a model, evaporation at any film portion causes the instant film edge receding, which assumes implicitly a hydrodynamic flow along the film. More advanced liquid film model has been proposed by Senjaya and Inoue (2013b) (their film flow equation was however incorrect, see Nikolayev and Sundararaj (2014) for the correct equation): the film was divided into finite elements of a fixed length and the film thickness variation due to both phase change and flow along the film was modeled. Although such a film description can be more accurate, it requires a much larger calculation effort because of an extra partial differential equation and management of the variable number of elements that depends on the bubble length.

A less complex approach was applied by Chauris *et al.* (2015); d’Entremont and Thome (2015b) who used the wedge film model proposed initially by Thome *et al.* (2004). This model is a variable ΔT version of the model that led to Eq. (25). The film flow (which is anyway small in the major film part) is neglected; the film thickness varies due to the phase change. At film deposition, $\delta = \delta_0$ is defined by the receding meniscus velocity (via an expression similar to Eq. (1)), which thus provides an initial condition. After deposition, the film thickness at a wall point x varies following Eqs. (23-24), where both $T_w(x)$ and $T^i = T_{\text{sat}}$ can vary in time. A minimum thickness of the order of surface roughness was imposed to avoid the divergence of evaporation rate $\sim \delta^{-1}$. When the film attains this minimum thickness, its evaporation stops. Such a model is capable of capturing the film slope effect described in sec. 3.3.3 but requires resolution of an extra equation on a fine wall mesh. For these reasons it is much more complex than the FEC model. It also neglects the CL effects (see sec. 2.3), exaggerates the film length and thus the film heat exchange. The constant thickness film hypothesized in the FEC model seems to be more adequate.

In the extension of FEC model proposed by Rao *et al.* (2017), the CL contribution to the evaporation flux was introduced together with the thinning of the film of homogeneous thickness. Rao *et al.* (2015) have managed to estimate experimentally the separate contributions of the film U_f and CL U_{cl} heat transfer. They used these data to account for the time variation of both spatially homogeneous film thickness and film length in the framework of the imposed temperatures boundary conditions. To describe the CL dynamics, instead of Eq. (50), they used an equation equivalent to

$$V_f = \begin{cases} V_m & \text{if } X_f \geq X_m, V_m < 0, \\ \dot{m}_{f, \text{cl}, e} / [\rho \pi d_i \delta(t)] & \text{otherwise,} \end{cases} \quad (77)$$

where the evaporation rate at CL in evaporator was

$$\dot{m}_{f,cl,e} = \begin{cases} \frac{U_{cl}}{h_{lv}} \pi d_i \delta(t) [T_e - T_{sat}(p)] & \text{if } X_f < L_e, \\ 0 & \text{otherwise.} \end{cases} \quad (78)$$

The variation of film thickness followed the law

$$\dot{\delta} = -\frac{\dot{m}_{f,e}}{\rho \pi d_i L_{f,e}}, \quad (79)$$

where $m_{f,e}$ is defined by Eq. (51) where $U_f = \lambda/\delta(t)$; $L_{f,e} = L_{f,e}(t)$ is related to X_f via Eq. (53). Eq. (79) is completely equivalent to Eqs. (23-24). For this reason this model presents a better alternative to the original FEC model. In addition, according to Eq. (77), the CL position changes because of the local CL evaporation and not because of the film overall evaporation postulated in FEC model. Therefore, the liquid flow along the film is absent, in agreement with the thin film theory discussed in sec. 3.3. An example of the PHP dynamics calculated with such an approach is shown in Fig. 24.

However, the CL dynamics equation (77) can still be improved. One should update it with the results of micro-scale modeling as discussed in sec. 3.3.5 to describe correctly the film shape and especially length strongly influenced by the dewetting effect. This is one of the main future challenges for the PHP modeling.

In spite of the above mentioned deficiencies, the FEC model is justified in situations where the film thickness variation during an oscillation period is not strong, i.e. $2\pi\dot{\delta}/\omega_0 \ll \delta$, where $\dot{\delta}$ can be estimated with Eq. (79). Among the existing approaches, the extended FEC model of Rao *et al.* (2017) is probably the best candidate for the next generation of multi-branch PHP models.

5. Two-branch PHP

Two kinds of the two-branch PHP are possible. The first is open U-tube (cf. sec. 2.3) with the vapor bubble (and the evaporator section) in the middle and both ends (two condenser sections) connected to a liquid reservoir maintained at constant pressure. Its functioning is almost similar to two single branch PHPs and for this reason will not be discussed any more. We will address instead a closed U-tube with a liquid plug in the middle and two vapor bubbles located in the closed tube ends (Fig. 27) with no adiabatic section. The motion of the plug in the two-branch PHP was considered first by Zhang *et al.* (2002) who implemented the superheated vapor model for the case of imposed evaporator and condenser temperatures. The momentum equation stems from Eq. (13) with the replacement $p = p_1$ and $p_{next} = p_2$, the pressures in the vapor bubbles 1 and 2,

$$\rho \frac{d(L_1 \dot{X}_m)}{dt} = p_1 - p_2 - 2\rho g X_m, \quad (80)$$

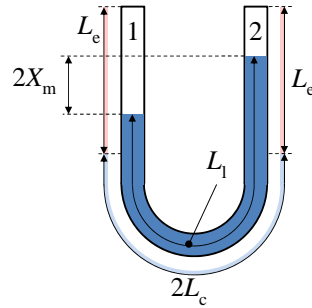


Fig. 27. Two-branch PHP.

The pressure losses related to the viscous effects and U-turn are omitted here for simplicity. The vapor pressures are related to the vapor masses and displacements with the expressions that can be obtained from Eqs. (17, 21):

$$p_i = p_0 \left(\frac{T_0 m_i R_v}{p_0 (L_0 \pm X_m) S} \right)^\gamma, \quad (81)$$

where p_0 , T_0 , and $L_0 = L_e + L_c - L_l/2$ are the equilibrium (i.e. for $X_m = 0$) values of pressure, temperature and vapor bubble length, respectively. The + and – signs correspond to $i = 1, 2$, respectively. Two equations for the vapor masses $m_{1,2}$ similar to Eq. (47) close the problem. Within such a statement, Zhang *et al.* obtained stable self sustained quasi-sinusoidal oscillations. The same problem statement was applied by Pai *et al.* (2013) who attempted an analytical approach based on multiple scales approximation similar to the averaging approximation mentioned in sec. 4.5. They gave an expression for the eigenfrequency of small-amplitude oscillation for the inviscid liquid plug in the two-branch PHP:

$$\omega_0 = \sqrt{\frac{2\gamma p_0}{\rho L_l \bar{L}_v} + \frac{2g}{L_l}}. \quad (82)$$

This expression can be compared to its single-branch PHP counterpart (70). One can see that the expressions are the same if one counts $L_l/2$ liquid plug length per branch. It is interesting to compare this expression to that of Newton (1687) who was the first to derive the oscillation frequency for the *open* U-tube. In addition to the Newton term $2g/L_l$, Eq. (82) includes a contribution from the adiabatic gas compression proper to the *closed* U-tube.

Yuan *et al.* (2010) repeated almost identically the simulation of Zhang *et al.* by using the 4th order Runge-Kutta method with very similar results.

A step forward has been done by Dilawar and Pattamatta (2013) who applied a simplified version of the FEC model: the moving contact lines were not implemented and continuous liquid films of constant thickness (cf. sec. 4.2) were postulated. The same problem with imposed evaporator and condenser temperatures was considered. They have also obtained the stable oscillation and studied the influence of different

parameters on the amplitude of the stable oscillations. In particular they added into the system the adiabatic section between condenser and evaporator. They found that the amplitude strongly decreased with L_a . They also introduced the dynamic contact angle hysteresis via the additional pressure drop proportional to the surface tension and depending on the direction of plug motion. They have found that this effect is negligible. As for the effect of the pressure drop at the bend, it was quite small. The effect of the orientation on the amplitude was also small, probably due to the strong contribution of the vapor compression. They compared three different liquids and found that the water and n-pentane performed better than ethanol.

Nagasaki *et al.* (2011) have performed an experiment on two-branch PHP in the imposed P_e mode and made a comparison with a theory based on the FEC model with the imposed T_e . They used δ and the film form factor to fit their data on the meniscus oscillation amplitude A , amplitude of pressure oscillation, mean pressure, and ω . They were able to fit some parameters while for the others, the fit was of average quality.

We note that the studies of the two branch PHP are still insufficient. No start-up analysis is available in the literature. However, in order to understand which mechanism is dominant in the multi-branch PHP, it is important to compare the instability threshold associated to the pressure imbalance in the branches to the instability mechanism of the single branch PHP.

All the modeling has been done for the case of imposed evaporator and condenser temperatures. We remind that for this kind of thermal boundary conditions, the liquid heat exchange does not impact the meniscus dynamics, which is not realistic at least for the start-up simulation as we saw on the example of the single-branch PHP. The theoretical studies of two branch PHP were carried out mostly for one filling ratio where the equilibrium meniscus position situates exactly on the border between condenser and evaporator.

5.1. Heat transfer via PHP

In the steady regime, the heat balance of PHP, as a thermal system, can be obtained from Eq. (59) by integrating it over x and averaging over t . The transient term vanishes (because of stationarity on average) and the total heat power P_e becomes equal to the power

$$\dot{Q}_e = \pi d_i \sum_k \int_{e,k} q_{\text{fluid}}(x) dx + S_w \sum_k (q_{w,e,k}^r - q_{w,e,k}^l) \quad (83)$$

transferred from the evaporator to the fluid (first term) and through the tube wall (second term) towards the adiabatic sections to the right and to the left of evaporator in the case of the multi-branch PHP. Here, $q_{w,e,k}^l$ and $q_{w,e,k}^r$ are the axial heat fluxes transferred through the tube at the evaporator left and right ends, respectively. The k -summation is performed over all the evaporator sections. The integration is performed over each section. In the case of the single branch PHP,

there is only one evaporator section and $q_{w,e,1}^l = 0$ according to the condition (65). A comparison of P_e and calculated \dot{Q}_e needs to be done to evaluate the coherency of simulation. In the case of the imposed constant temperatures of both evaporator and condenser, to check the simulation coherency, one needs to compare \dot{Q}_e to the power

$$\dot{Q}_c = \pi d_i \sum_k \int_{c,k} q_{\text{fluid}}(x) dx + S_w \sum_k (q_{w,c,k}^r - q_{w,c,k}^l) \quad (84)$$

dissipated in the condenser. Since the heat losses in the adiabatic section are usually neglected, this quantity should be equal to \dot{Q}_e .

The issue of the latent versus convective heat transfer remains a subject of active discussions since the emergence of first PHP simulations. The latent heat contribution to the evaporator power is

$$\dot{Q}_e^{\text{lat}} = \pi d_i \left\{ \sum_i \int_{e,f,i} U_f [T_w(x) - T_{\text{sat}}] dx + \sum_n U_m L_m [T_w(X_m^n) - T_{\text{sat}}] \right\}. \quad (85)$$

Integration in the first term is performed over the length of the films of the i -th bubble belonging to an evaporator section. The second term is the sum over all the menisci with the positions X_m^n belonging to all evaporator sections. The sensible heat transfer in the evaporator can be described by a similar expression

$$\begin{aligned} \dot{Q}_e^{\text{sen}} = \pi d_i \sum_i \left\{ \int_{e,v,i} U_v [T_w(x) - T_i] dx + \int_{e,l,i} U_l [T_w(x) - T_l(x)] dx \right\} \\ + S_w \sum_k (q_{w,e,k}^r - q_{w,e,k}^l). \end{aligned} \quad (86)$$

corresponding to the dry area inside the i -th bubble, the i -th liquid plug and the heat conduction via the tube itself. The expressions for the latent and sensible heat exchange contributions to the power transferred to the condenser are very similar and we will not write them.

In practice, summation over the bubbles is more convenient than the summation over evaporator sections, so instead of using Eq. (83), one applies Eqs. (85, 86) and then calculates $\dot{Q}_e = \dot{Q}_e^{\text{lat}} + \dot{Q}_e^{\text{sen}}$.

6. Genesis of multi-branch simulation modeling

6.1. Superheated vapor modeling

Most of the PHP simulations are one dimensional (1D). The reasons for such a choice is the relative simplicity on one hand and the capability to describe the relevant physical phenomena, on the other. In their pioneering approach, Shafii *et al.* (2001) introduced basic principles for the 1D modeling. Either vapor bubble with continuous films on the walls or liquid plug are assumed to occupy all the tube cross-section (no dispersed flow). The PHP meander is represented by a straight

tube with periodic boundary conditions; the PHP periods containing evaporator, adiabatic, condenser and again adiabatic sections follow each other sequentially (Fig. 28). The number of such periods N_p is the main geometrical parameter (called also the number of PHP turns). In the work of Shafii *et al.*, it is equal to three. The feedback section (a vertical section in Fig. 28) is not simulated ($L_{fb} = 0$). Each bubble and its next plug are identified by the index $i = 0, \dots, M - 1$. The left end of the plug is thus X_i^r and the right is $X_{next,i}^l$, where $X_{next,i}^l = X_{i+1}^l$ unless $i = M - 1$, in which case $X_{next,i}^l = X_0^l$.

The total number M of bubble-plug couples may change in time because of plug coalescence. The equations of motion are the sequential versions of the superheated vapor model equations (13, 47, 37) (see sec. 4.1)

$$\frac{d}{dt}(m_{l,i}V_i) = (p_i - p_{next,i})S - F_i + G_i, \quad (87)$$

$$\dot{m}_i = \frac{\pi d_i}{h_{lv}} [U_e L_{v,e,i}(T_e - T_i) + U_c L_{v,c,i}(T_c - T_i)], \quad (88)$$

$$\dot{X}_i^r = \dot{X}_{next,i}^l = V_i, \quad (89)$$

where V_i is the i -th plug center of mass velocity and F_i is given by Eq. (12). Two more equations corresponding to (17, 21) have to be added to describe the vapor thermodynamics:

$$p_i S L_{v,i} = m_i R_v T_i, \quad (90)$$

$$p_i = p_{0,i} \left(\frac{T_i}{T_{0,i}} \right)^{\frac{\gamma}{\gamma-1}}, \quad (91)$$

$$(92)$$

where the indexes $0, i$ identify the initial state of the i -th bubble.

To provide the mass conservation in the tube, they subtract from a plug a half

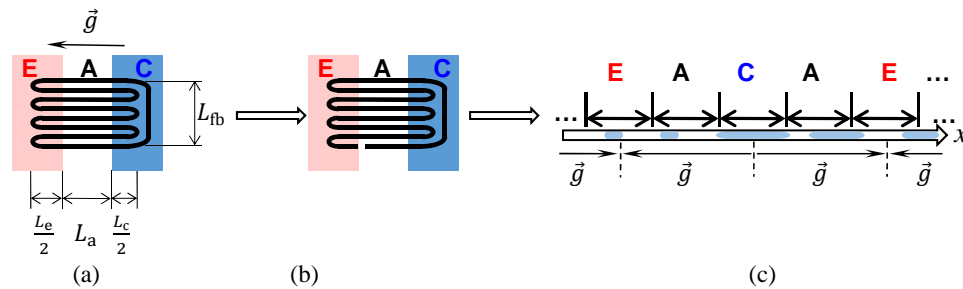


Fig. 28. (a) Closed loop PHP of a simple geometry and the gravity direction. The number of turns $N_p = 4$ here. (b,c) Geometrical transformations of the tube. (b) Unlooping (c) Unbending and projection to the x axis. The splitting of the x axis to branches is shown together with the gravity direction in each branch.

of fluid mass evaporated to two neighboring bubbles:

$$\dot{m}_{l,i} = -\frac{1}{2}(\dot{m}_i + \dot{m}_{i+1}). \quad (93)$$

One notices that, Eq. (89) lacks consistency as the plug mass change but both the liquid density and the liquid plug length are constant. Such an approach can work provided the evaporated mass over an oscillation period remains small with respect to the plug length. The PHP looping was enforced via correction after each time step of the positions of menisci when they go beyond the limits $[0, L_t]$, where is the total length measured along the PHP tube. If a meniscus position X_i^s (with $s = r$ or l) becomes to be larger than L_t , it is replaced by $X_i^s - L_t$. When it becomes smaller than zero, it is replaced by $X_i^s + L_t$.

The simulation resulted in a steady oscillation regime after a transient during which the number of liquid plugs dropped from initially imposed larger number to N_p . During oscillations, the liquid remained in the condenser bends, while the vapor persisted in the evaporator bends. The steady regime was attained. The oscillations of menisci were periodical and nearly sinusoidal, with the amplitude $\approx 0.15L_e$. In other words, the multi-branch PHP acted like an assembly of oscillators (two-branch PHPs) coupled through the vapor pressure in each bubble separating them. We call this regime small amplitude oscillations as the liquid plugs never transit through the evaporator bends.

Sakulchangsattajai *et al.* (2004) compared the overall heat transfer (described in sec. 5.1) of the model of Shafii *et al.* with the existing experimental data and concluded that the agreement was satisfactory. However they did not mention their simulation parameters, in particular, the most important heat transfer coefficients U_e and U_c .

Holley and Faghri (2005) introduced the tube heat conduction and its thermal coupling with the fluid (see sec. 4.2.2). This a very important milestone because that changes in particular the start-up criteria. However the vapor energy equation they used was incorrect, see sec. 3.2.2. Mameli *et al.* (2012) introduced into their code the pressure losses in the turns (see sec. 3.1.2).

Peng *et al.* (2014) implemented the superheated vapor model for several working fluids for eight-turn PHP. For U_e and U_c , they took the flow boiling heat transfer coefficient that is generally much larger than the film heat transfer coefficient. The justification for this choice is not given. They simulated three different fluids: ammonia, water and acetone. The oscillation regime was mainly chaotic with the bottom heated mode and weak sinusoidal oscillations in horizontal orientation. One of their aims was to verify if the circulation regime is described by their model. The circulation regime corresponds to the nonzero average velocity of all liquid plugs. This regime is very desirable in PHP because the heat transfer in it is believed to be maximal. When choosing the circulation initial conditions for ammonia they indeed observed the continuing circulation. They however simulated a short period of time where the average values of their system variables varied and the steady

regime (cf. sec. 4.4 for its definition) was hardly attained. The circulation regime was not possible in the horizontal PHP orientation.

Very recently, [Yoon and Kim (2017)] implemented the superheated vapor model for the five-turn ethanol-filled PHP in the bottom-heated orientation. They obtained small-amplitude oscillations, which they also observed experimentally.

6.2. FEC model: imposed temperatures

Nikolayev (2011b) generalized the FEC model (sec. 4.2.1) to the multi-branch PHP for the imposed temperatures in evaporator and condenser and arbitrary L_a . In addition, several simulation algorithm improvements have been proposed to make the simulation more robust. Until this work, the explicit time marching scheme was used to solve the set of differential evolution equations. This (Euler) method is known to be numerically unstable, which may cause artificial oscillations that can be confused with the true physical oscillations. As the core solver algorithm, Nikolayev introduced the 4th order Runge-Kutta method renowned for its numerical stability. This added complexity in the management of PHP dynamics associated with appearance or disappearance of its components like vapor bubbles or liquid plugs. Such system changes (called events hereafter) lead to a change in the number of variables and for this reason require a restart of calculation of the time step after detection of an event. It was also proposed to keep all the information on the current state of the bubble-plug couple within a unique data structure and use the dynamic memory allocation (reserving-liberating the computer memory at runtime). This is more convenient than reserving statically (at the compilation stage) fixed memory amount with a risk of an overflow because an extra liquid film or bubble required during the simulation. The introduction of discontinuous liquid film necessitated an advanced management of the fluid mass conservation, in particular, the account of plug mass reduction during its advancing over the dry evaporator wall; the trailing plug meniscus always deposited the liquid film. Unlike the Shafii *et al.* model (cf. Eq. (89)), the plug mass change rate $\dot{m}_{l,i}$ that accounted for the meniscus evaporation terms similar to (55) and for the film deposition and absorption impacted the velocities of menisci

$$\dot{X}_i^r = V_i - \frac{\dot{m}_{l,i}}{2\rho S}, \quad (94)$$

$$\dot{X}_{\text{next},i}^l = V_i + \frac{\dot{m}_{l,i}}{2\rho S}. \quad (95)$$

Several dry areas per bubble and, accordingly, several film pairs are allowed. The management of PHP looping is different from Shafii *et al.* because of a large number of coordinate variables per bubble (film edge coordinates). Within the approach of Shafii *et al.*, they would need to be corrected at each time step to make them belong to the interval $(0, L_t)$. Instead, all the bubble-plug “train” is allowed to displace freely along an infinite axis. One needs to enforce only the looping condition. It

says that the right meniscus position of the M -th (last) liquid plug is equal to the left meniscus position of the first bubble plus L_t . To find out to which section a coordinate x belongs, one needs to reduce x by finding a remainder of division by L_t .

A horizontal water-filled PHP was simulated. Developed oscillations were obtained. Several regimes have been identified depending on the difference $T_e - T_c$. At small $T_e - T_c$ an initial system perturbation declined in time. At larger $T_e - T_c$, intermittent oscillations appeared where the intervals of strong oscillations alternated with the intervals of weak oscillations. At a critical value of $T_e - T_c$, the weak oscillations disappeared and the oscillations were strong all the time; this regime was called chaotic. Beginning from some upper critical threshold, all the liquid plugs coalesced into one large plug and the motion stopped. This latter regime is nonphysical. In the experiment, the bubbles would nucleate and grow in the liquid plug portion situating in the evaporator cutting the large plug into smaller parts. However the bubble generation was not implemented.

6.3. Bubble generation model by Senjaya and Inoue

The vapor bubble generation was first introduced by Senjaya and Inoue (2013b). Their model describes a generation of “tube-size” bubbles, i.e. bubbles of a small length that occupy all the tube cross-section. This is the only option in a 1D model. The bubbles of the length $L_{\text{nuc}} = 1$ mm are assumed to nucleate at several nucleation sites (typically, one per branch) under two simultaneous conditions justified by their experimental observations. The first condition is conventional

$$T_w - T_{\text{sat}}(p) > \Delta T_{\text{nuc}} \quad (96)$$

and means that the wall superheating exceeds a nucleation barrier $\Delta T_{\text{nuc}} \sim 5 - 10^\circ$, which is a typical nucleation barrier in boiling. The newly nucleated bubble pressure p is equal to the liquid pressure at the nucleation site location. The liquid pressure is assumed to vary linearly along the plug,

$$p_{l,i}(x) = p_i + (p_{\text{next},i} - p_i) \frac{x - X_i^r}{L_{l,i}}. \quad (97)$$

The second condition of nucleation is a limitation on the liquid plug velocity, $|V_i| \leq 0.2$ m/s. This value is based on the detailed experimental observations [Senjaya and Inoue (2013a)] of bubble generation in the transparent evaporator of a horizontal PHP. The tube-size bubble are observed to appear as a result of growth and coalescence of small diameter bubbles, which nucleate and grow at the hot tube wall. If the plug velocity is small enough, the small bubbles grow and coalesce to form tube-size bubbles during plug residence in the evaporator. If the plug velocity is large, the small bubbles easily detach from the wall and does not grow nor coalesce. The tube size bubble is not formed and the small bubbles are recondensed when the plug enters the condenser. In the model, liquid films are assumed to be

continuous at the bubble formation. The film evaporation model is close to the FEC model (sec. 4.2.1) with imposed condenser and evaporator temperatures. The authors do not discuss the minimal distance $L_{\text{nucl},\text{min}}$ from the end of the plug at which the bubbles are allowed to nucleate. Apparently, it was introduced: when a plug approaches the nucleation site inside the evaporator, the pressure is the smallest at the leading plug meniscus so the criterion (96) is satisfied right *at* the meniscus. However the nucleation should occur *inside* the plug so $L_{\text{nucl},\text{min}}$ should be necessarily introduced. Physically, it corresponds to the time (multiplied by the meniscus velocity) needed to form a thermal boundary layer in which the bubble is nucleated inside the liquid.

Another particularity of the model is an assumption of faster growth of the newly nucleated bubbles: the evaporation film heat exchange coefficient U_f was imposed to be ten time larger than for the rest of the bubbles. For smaller multipliers, the liquid plug oscillations were small and sinusoidal like in the Shafii *et al.* simulation; it did not attain the nucleation site and the bubble generation did not occur.

Ethanol filled PHP with no adiabatic section was simulated. With no bubble generation, only small amplitude sinusoidal oscillations appeared. With the bubble generation, the amplitude of oscillation was much larger. Senjaya and Inoue (2013c) performed an analysis of bubble generation parameters. In particular, they showed a strong dependence (increase) of the PHP performance on the number of nucleation sites. This is a deficiency of their model since in reality, this number is large so there should be a saturation. In their model, the number of liquid plugs tends to be the same as the number of turns, similarly to the Shafii *et al.* simulation. In their model, Senjaya and Inoue (2014) also discussed the film drying in evaporator. In their model the dryout did not occur when the bubble generation was present.

6.4. Simulation of d'Entremont and Thome

One of the most advanced PHP simulation approaches was developed by d'Entremont and Thome (2015a,b), first of all due to the variable thickness wedge film model discussed in sec. 4.7. The 4th order Runge-Kutta method was used for the time stepping. This model is for $L_a = 0$ and the imposed constant temperatures of both evaporator and condenser. An extensive regime analysis has been performed for the R245fa fluid for different fill ratios and number N_p of turns ranging from 1 (looped thermosyphon) to 24. The main functioning regime was small amplitude chaotic oscillations of large liquid plugs, one plug per turn in condenser section. The bubble generation was introduced. Instead of choosing fixed nucleation sites, a bubble was nucleated at a location of maximum liquid superheating that was searched inside each plug. Two its portions of the length $L_{\text{nucl},\text{min}} = 2$ mm adjacent to the menisci were excluded from the search. Once a large plug penetrated into the evaporator and the criterion (96) was satisfied, a bubble was nucleated. Since the evaporator wall temperature was constant, the bubble was nucleated always at the distance $L_{\text{nucl},\text{min}}$ from the leading plug meniscus (see a discussion in sec. 6.3) since

the superheat attained its maximum there. This means that a small liquid plug of the fixed length $L_{\text{nucl,min}}$ was cut by the nucleated bubble from the large plug. This small plug was propelled by the expanding bubble into the evaporator. While moving, the small plug left behind a liquid film thus shrinking in length. Typically, the small plug disappeared before crossing the whole evaporator. But sometimes it reached the opposite large plug and coalesced with it thus increasing temporarily the oscillation amplitude. According to the results of d'Entremont and Thome, the bubble generation introduced a perturbation to the motion of the large plugs that oscillated each in its own condenser.

The two-turn PHP showed oscillations in the favorable vertical orientation (evaporator at the bottom). Probably under the action of gravity the average position of the liquid plugs in the condenser sections was shifted to one of the sides (both plugs to the same side). For this reason, they entered the condenser more often from one side than from another, which caused the birth and dissymmetric propulsion of the small plugs preferentially in one direction so the average plug velocity was nonzero. They called such a regime circulation (the major part of the liquid did not circulate though). Such a dissymmetry was nonexistent at larger turn number, with reduction of the heat transfer rate per turn. The two branch PHP did not oscillate in horizontal nor in inverted position. The critical N_p for (nearly) gravity-independent functioning situated between 5 and 15 depending on the temperatures.

However the vapor thermodynamic model of d'Entremont and Thome (2015a,b) assumed that the vapor is always at saturation which is hardly justified in the PHP case, see sec. 3.2.1 for the discussion.

6.5. FEC model with tube heat conduction

A study of the single-branch PHP (sec. 4.6) suggests the impact of the wall heat conduction may be strong also for the case of the multi-branch PHP. Nekrashevych and Nikolayev (2017) further developed the FEC model of Nikolayev (2011b) to include the effects of wall heat conduction and bubble generation. The heat power was homogeneously injected into the tube walls within the evaporator section while the temperature of the internal tube walls was imposed in the condenser section. Some other features were added, like the arbitrary length L_{fb} of the feedback section (see Fig. 28) and the pressure loss at the bends (see sec. 3.1.2). To implement the FEC model, notions of the effective evaporator and condenser had to be generalized to the case of multi-branch PHP where the temperature distribution along a bubble can be non-monotonous. Because of this, several dry areas per bubble and, accordingly, several film pairs can appear. Their left and right edge positions are denoted with $X_{\text{f},i}^{1,k}$ and $X_{\text{f},i}^{r,k}$ for the k -th pair, cf. Fig. 29. The effective evaporator is a part of the wall inside the bubble i which is either dry or along which $T_w > T_{\text{sat},i} \equiv T_{\text{sat}}(p_i)$. The variable number of effective evaporators is denoted $N_{\text{e},i}$ and their left and right borders as $X_{\text{e},i}^{1,k}$ and $X_{\text{e},i}^{r,k}$, respectively. The management of PHP looping is similar to that described in sec. 6.2. It stems from such a formulation that the following

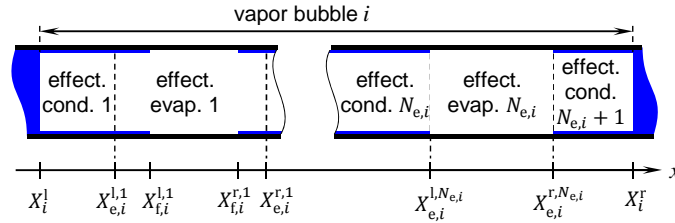


Fig. 29. Geometry of the effective evaporators and condensers. Both liquid and liquid films are shown in blue. In this example, $X_{f,i}^{l,N_{e,i}} = X_{f,i}^{l,N_{e,i}}$ and $X_{f,i}^{r,N_{e,i}} = X_{e,i}^{r,N_{e,i}}$.

inequalities are satisfied for each bubble i : $X_i^l \leq X_{e,i}^{l,1} \leq X_{f,i}^{l,1} \leq X_{f,i}^{r,1} \leq X_{e,i}^{r,1} \leq \dots \leq X_{e,i}^{l,N_{e,i}} \leq X_{f,i}^{l,N_{e,i}} \leq X_{f,i}^{r,N_{e,i}} \leq X_{e,i}^{r,N_{e,i}} \leq X_i^r$.

Introduction of $X_{e,i}^{l,k}$ and $X_{e,i}^{r,k}$ is necessary for separate calculation of the evaporation film rates from left and right films

$$\dot{m}_{f,e,i}^{r,k} = \frac{U_f \pi d_i}{h_{lv}} \int_{X_{f,i}^{r,k}}^{X_{e,i}^{r,k}} (T_w(x) - T_{sat,i}) dx, \quad (98)$$

$$\dot{m}_{f,e,i}^{l,k} = \frac{U_f \pi d_i}{h_{lv}} \int_{X_{e,i}^{l,k}}^{X_{f,i}^{l,k}} (T_w(x) - T_{sat,i}) dx. \quad (99)$$

used for the definition of the film edge dynamics below. These equations are the multi-branch counterparts of Eq. (58). The vapor mass change of the i -th bubble caused by the condensation in the k -th effective condenser is

$$\dot{m}_{f,c,i}^k = \frac{U_f \pi d_i}{h_{lv}} \begin{cases} \int_{X_i^l}^{X_{e,i}^{l,k}} (T_w(x) - T_{sat,i}) dx, & \text{if } k = 1 \\ \int_{X_{e,i}^{r,k-1}}^{X_{e,i}^{l,k}} (T_w(x) - T_{sat,i}) dx, & \text{if } 1 < k \leq N_{e,i} \\ \int_{X_{e,i}^{r,k-1}}^{X_i^r} (T_w(x) - T_{sat,i}) dx, & \text{if } k = N_{e,i} + 1 \end{cases} \quad (100)$$

The vapor mass change of the i -th bubble caused by the s -th ($s=1,r$) meniscus phase change is (cf. Eq. (55))

$$\dot{m}_{m,i}^s = \frac{U_m \pi d_i L_m}{h_{lv}} [(T_w(X_i^s) - T_{sat,i})], \quad (101)$$

The total phase change rate for the i -th bubble (cf. Eq. (54))

$$\dot{m}_i = \dot{m}_{m,i}^l + \dot{m}_{m,i}^r + \dot{m}_{f,c,i}^{N_{e,i}+1} + \sum_{k=1}^{N_{e,i}} (\dot{m}_{f,e,i}^{l,k} + \dot{m}_{f,e,i}^{r,k} + \dot{m}_{f,c,i}^k) \quad (102)$$

is a sum of masses taken from films (and also menisci) per second.

The film dynamics is described by the multi-branch counterparts of Eq. (50),

$$\dot{X}_{f,i}^{r,k} = \begin{cases} \dot{X}_i^r, & \text{if } X_{f,i}^{r,k} \geq X_i^r \text{ and } \dot{X}_i^r \leq 0 \\ \dot{X}_i^l, & \text{if } X_{f,i}^{r,k} \leq X_i^l \text{ and } \dot{X}_i^l \geq 0 \\ \frac{\dot{m}_{f,c,i}^{k+1}}{2\rho\pi d_i \delta}, & \text{if } X_{e,i}^{r,k} \leq X_{f,i}^{r,k} \text{ and } X_{f,i}^{l,k} < X_{f,i}^{r,k} \\ \frac{\dot{m}_{f,e,i}^{r,k}}{\rho\pi d_i \delta}, & \text{otherwise.} \end{cases} \quad (103)$$

$$\dot{X}_{f,i}^{l,k} = \begin{cases} \dot{X}_i^l, & \text{if } X_{f,i}^{l,k} \leq X_i^l \text{ and } \dot{X}_i^l \geq 0 \\ \dot{X}_i^r, & \text{if } X_{f,i}^{l,k} \geq X_i^r \text{ and } \dot{X}_i^r \leq 0 \\ -\frac{\dot{m}_{f,c,i}^k}{2\rho\pi d_i \delta}, & \text{if } X_{e,i}^{l,k} \geq X_{f,i}^{l,k} \text{ and } X_{f,i}^{l,k} < X_{f,i}^{r,k} \\ -\frac{\dot{m}_{f,e,i}^{l,k}}{\rho\pi d_i \delta}, & \text{otherwise.} \end{cases} \quad (104)$$

The order of lines is meaningful (2nd option holds if the 1st is invalid, the 3rd if first two are invalid, etc.). The 1st line means the absence of the film (which implies $\dot{m}_{f,c,i}^k = \dot{m}_{f,e,i}^{s,k} = 0$) and the meniscus advancing motion. The 2nd line means the dry spot absence and the absence of the opposite film, the film junction point situating at the opposite meniscus. These lines are introduced to avoid leaving the film edges outside the bubble. The 3rd line corresponds to the film edge advancing motion because of condensation when the whole film is in the effective condenser. Only a half of the condensed mass contributes to the left film elongation; the other half is used for the elongation of the right film of the dry spot $k + 1$. The 4th line corresponds to the film edge retraction when the film edge is within the effective evaporator.

The numerical software that implements this algorithm is called CASCO (Code Avancé de Simulation de Caloduc Oscillant: Advanced PHP simulation code in French). A postprocessor of the CASCO data files is called PHP_Viewer (Fig. 30). It visualizes the PHP dynamics by showing the position of the menisci and film edges and also can visualize the temperature distributions in the PHP walls and liquid plugs.

The simulations have shown the absence of the PHP start-up without bubble generation. Whatever is P_e , the oscillation starts initially but chain bubble coalescence occurs and, eventually, all the liquid gathers in a single plug; its oscillations decline quickly. This seems to be an effect of the tube heat conduction. One thus needs to account for the bubble generation. The PHP starts-up smoothly, without the evaporator temperature overshoot (i.e. peak) before the beginning of oscillations.

The bubble generation algorithm is similar to that of d'Entremont and Thome (2015a,b) with a notable difference: the wall temperature spatially varied (Fig. 31).

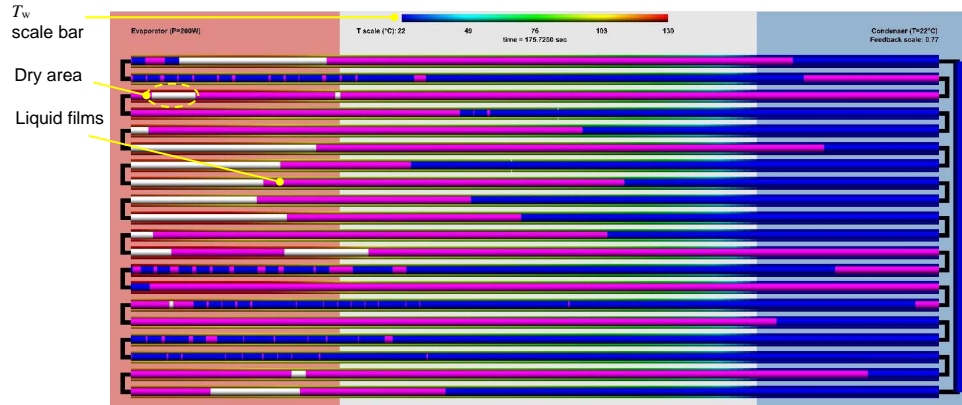


Fig. 30. The PHP geometry representation by the PHP_Viewer post-processor of the CASCO data files. It shows an example of the 10-turn water-copper PHP for $T_c = 22^\circ \text{C}$ and $t \simeq 175 \text{ s}$ since $P_e = 200 \text{ W}$ switching. Thin liquid films (in violet) cover the internal tube walls inside of the vapor bubbles, except of the dry spot areas (white). The liquid plugs are shown in blue. The wall temperature is shown with the color varying from blue to red; the T_w scale is indicated at the top. The round turns are not drawn for simplicity; black lines just connect equivalent points that correspond to the extreme points of each turn.

For this reason, the bubbles can nucleate wherever the nucleation criterion is satisfied, not necessarily at the evaporator boundary. If the wall is hot enough, many

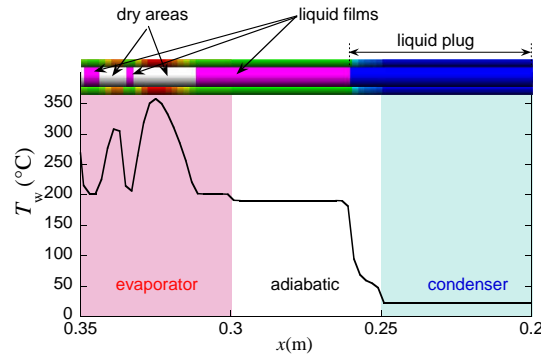


Fig. 31. An example of the temperature distribution shown both by the curve and color variation along the PHP tube during dryout regime simulation for $t = 4 \text{ s}$ since $P_e = 360 \text{ W}$ switching) of the 5-turn water filled hastelloy PHP. The same branch is indicated by an arrow in Fig. 34 below. One can see T_w drop in the film-covered tube areas because of the film evaporation and T_w rise in the dry areas [Nekrashevych and Nikolayev (2017)].

bubbles may be generated one after another at the same hot spot so “bubble trains” are formed until the hot spot is cooled down, cf. Fig. 32.

This event can be seen in Fig. 33 where the time evolution of the left and right ends of many bubbles is shown for the same case as in Fig. 32. For any particular newly born bubble, one can easily identify the left and right bubble ends in Fig. 33

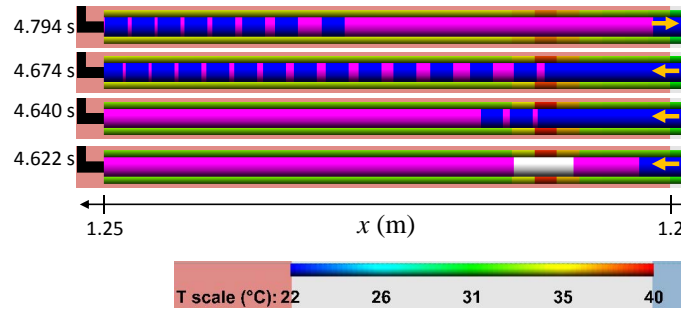


Fig. 32. An example of multiple bubble generation in the evaporator of the 9-th branch of 5-turn PHP at $P_e = 60$ W. As a result of the bubble generation, the hot (nucleation) spot is cooled down and the generation stops. Arrows show the direction of motion of the rightmost liquid plug [Reproduced from Nekrashevych and Nikolayev (2017)].

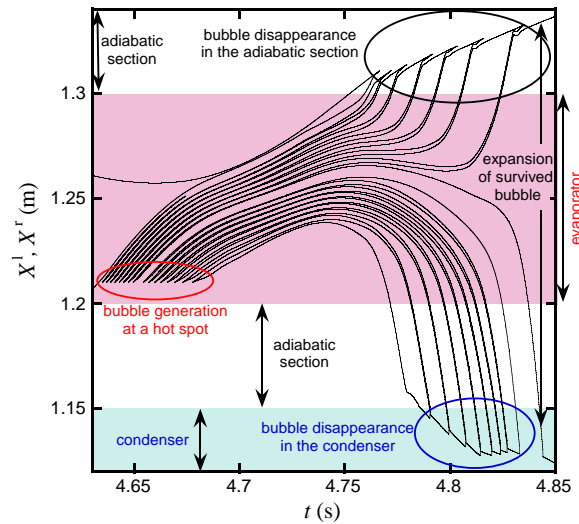


Fig. 33. Time evolution of bubble end coordinates in the 9th and 10th branches. Each pair of solid lines corresponds to a bubble, i. e. to the temporal variation of its X^l and X^r . Each starting (i.e. opening to the right) cusp point corresponds to the bubble generation at a hot spot. Each ending (i.e. opening to the left) cusp point corresponds to the bubble disappearance [Reproduced from Nekrashevych and Nikolayev (2017)].

because they form a divergent cusp point at the birth moment (encircled in red). As mentioned before, $X_i^l \leq X_i^r$ so the vertical distance between X_i^l and X_i^r curves defines the variable in time bubble length. The plug length (the distance between X_{i+1}^l and X_i^r) changes in time because of the meniscus phase change and because of the liquid film deposition by the receding plug meniscus if the other end advances along the dry wall.

Right after generation, the velocity of the bubble train coincides with that of

the parent plug. The growth of a bubble in evaporator causes compression of the neighboring bubbles and the direction of plug motion can be inverted (cf. Fig. 32 for $t = 4.794$ s). This inversion can also be seen in Fig. 33 where the slope of curves (defining the plug velocity) changes its sign. Such an inversion means an oscillation. This shows the mechanism of oscillation sustainment by bubble generation.

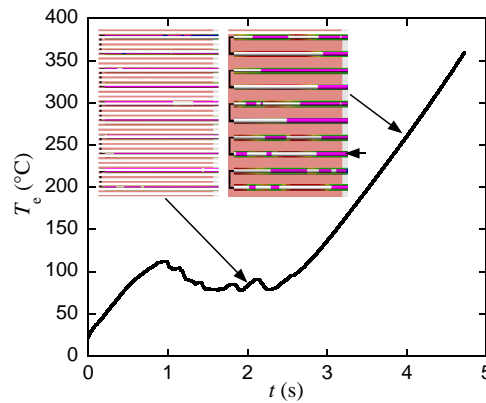


Fig. 34. Tube wall temperature for $P_e = 360$ W averaged over evaporator: dry-out dynamics. The images of evaporator are shown for two different times ($t = 2$ and 4 s) to illustrate the dry area growth dynamics [Reproduced from Nekrashevych and Nikolayev (2017)].

CASCO can simulate the complete PHP halt by dry-out that occurs when P_e exceeds a threshold. At the dryout, the film length decreases in the evaporator and large dry spots (white areas in the evaporator shown in Fig. 34) grow. The evaporator temperature rises. The fast film evaporation in evaporator leads to the pressure rise and all the liquid plugs are expelled almost simultaneously from the evaporator. Such an event causes strong compression of bubbles that situate in condenser and adiabatic sections. The vapor inside these bubbles condense until their complete disappearance. As a result, all the liquid gathers in the condenser while all the vapor is located in the evaporator.

The dry-out has been already simulated by [Senjaya and Inoue (2014)]. However, they could not obtain the dry-out with bubble generation. Nekrashevych and Nikolayev (2017) obtained the dry-out with bubble generation, in agreement with numerous PHP experiments where bubble generation is always present.

Daimaru *et al.* (2017b) implemented the FEC model in the version of continuous liquid films (no dry areas) for the multi-branch PHP, just like Dilawar and Pattamatta (2013) did for the two-branch PHP. The fluid-tube thermal interaction was implemented and the heat flux was homogeneously distributed along the tube in the evaporator section. The heat exchange boundary conditions were implemented in the condenser section, i.e. Eq. (64) was applied. The bubble generation was not implemented.

The PHP start-up was not smooth, i.e. the evaporator temperature exhibited a

peak before dropping when the oscillations begin. They were periodical, with one liquid plug per condenser bend. The system behaved as coupled nearly harmonic oscillators with a phase shift between oscillations of neighboring plugs.

The same team further improved their simulation code by implementing the liquid film drying (although within only one dry area per vapor bubble) and the bubble generation [Daimaru *et al.* (2017a)]. For the first time, they introduced into simulation the check valves and a simulation of the heat spreader that provided a thermal interaction between the different PHP branches as discussed in sec. 4.2.2. Daimaru *et al.* studied the start-up that occurred without the temperature overshoot and obtained a steady regime. Due to the check valves, they obtained a true circulation regime of PHP. The agreement with experimental data was fairly good. However they could not make a detailed comparison because the experimental data lacked: their experiment was performed on board of a satellite. Daimaru *et al.* also raised a very important question about the influence of the initial liquid plug distribution on the PHP start-up. They concluded that at low heating power the PHP would not start-up if the evaporator is initially dry. However, the start-up occurred under such a condition at a higher power.

7. 2D and 3D simulations of multi-branch PHP

The simulations in higher dimensions are much more intensive in terms of programming time and computer resources, and for this reason they are rarely found in the literature. Within such an approach, the full Navier-Stokes equations are solved. One needs to describe numerically the free liquid-gas interfaces, which requires a quite strong (both programming and computational) effort. In addition, a fine meshing is generally necessary to describe thin liquid films. All these issues mean a necessity of commercial CFD codes. As soon as two phase calculations with heat exchange are concerned, an issue of validity of commercial CFD codes arises; an extensive code benchmarking is required. Also these codes are often the “black boxes”, i.e. one is never sure what are the algorithms used by them.

Givler and Martinez (2009, 2013) used the commercial CFD code Flow-3D to model the PHPs of increasing complexity in 2D and later in 3D. An extensive simulation work has been carried out. The simulations are described in detail and the values of relevant parameters are discussed. The constant heat flux at the evaporator and constant T_c were imposed. The tube conduction was implemented. The liquid films are not modeled. The management of vapor is done according to a built-in model. Each bubble is described by a single temperature like in the 1D models discussed above. However, the saturation temperature at the meniscus is not imposed as a boundary condition. The vapor energy equation (Eq. (7) of Givler and Martinez (2013)) is incorrect similarly to those discussed in sec. 3.2.2.

A single-turn (closed loop) PHP was analyzed by using the ANSYS Fluent commercial software by Wang *et al.* (2015) in 2D. The fluid dynamics is solved in both

phases and the films are resolved. The bubble generation is implemented. The issue of nucleation barrier is not discussed. There is again a problem with the energy equation that stipulates that the latent heat is injected into one of the phases, see sec. 3.2.2. The PHP dynamics is chaotic and the flow pattern looks realistic.

Pouryoussefi and Zhang (2016b,a, 2017) performed an extensive study of 2, 4, and 5-turn PHP configurations in 2D. The approach is similar to that of Wang *et al.*. Dry area appearance is also described. The vapor EOS and energy equation are not clear. It is not clear which code was used for the simulations. The employed computer resources are not specified either. They are probably considerable.

To conclude this section, the 2D and 3D approaches present interesting alternatives to 1D approaches because they describe more precisely the different flow regimes like dispersed flow. However, such approaches are incomparably more demanding in computer resources and require mastering the CFD code used for the simulation to provide an adequate description of the energy transfer in the system.

8. Conclusions

In this chapter we reviewed the current state of PHP modeling. Because of non-stationary functioning of PHP, the heat transfer correlations appear to have a poor prediction capability. The PHP dynamic simulation seems to be the only way of its modeling and design. While the direct numerical simulation in 2D or 3D can accurately describe different flow regimes inside the PHP, 1D simulations appear as a viable and much less expensive alternative.

We must mention that, to obtain otherwise nonexistent oscillating solutions within oversimplified approaches, many models sacrifice the physics of vapor phase. By fitting the model parameters, it turns out to be possible to use such models to obtain reasonable agreement with system level experimental data. However, to obtain viable models suitable for modeling and design of industrial prototypes, one needs to begin with the physically justified assumptions. We reviewed the physical phenomena relevant for the PHP to show how their knowledge can help to improve the existing models. We hope that our work will be useful for scientists who will pursue the modeling work for the sake of present and future industrial applications of the PHP.

9. Acknowledgements

The authors would like to thank the European Space Agency for the support through the MAP INWIP AO-2004-096. MM would like to thank the European Space Agency also for the support through MAP ENCOM, AO-2004-096, and UK EP-SRC Grant EP/P013112/1. MM would like also to thank Prof. S. Chandra at the University of Toronto and Prof. A. Amirfazli at the York University in Toronto, Canada, for having granted to spend some time as Visiting Professor at their In-

stitutions. VN is grateful to all collaborators who contributed to the PHP related research during past years, especially Dr. Ph. Gully, Mr. E. Ercolani, Prof. J. Duplat, Dr. L. Fourgeaud, and Dr. I. Nekrashevych. The authors would also like to thank Dr. V. Ayel and Dr. M. Mameli for the continuous support and many discussions in the last years. VN is grateful to his colleagues: Prof. F. Lefevre, Prof. J. Bonjour, Prof. Y. Bertin, and Dr. C. Romestant for many fruitful discussions and collaborations. MM is thankful to Prof. S. Filippeschi, Dr. D. Mangini, Dr. N. Miche, Dr. A. Georgoulas, Dr. C. De Falco and Prof. L. Araneo, and all his Ph.D. students for the never-ending interest in pulsating heat pipes. VN thanks Dr. M. Rao for giving the data of one of his figures.

Nomenclature

| | |
|--------|------------------------------------------------------------------|
| ℓ | characteristic length scale [m] |
| A | meniscus oscillation amplitude [m] |
| C | viscous friction coefficient |
| c | specific heat [J/(kg·K)] |
| Ca | dimensionless capillary number |
| D | heat diffusivity [m ² /s] |
| d | dimensionless half-length of liquid volume element, diameter [m] |
| e | Euler number $\simeq 2.71 \dots$ |
| F | viscous friction force [N] |
| G | gravity force [N] |
| g | gravity acceleration [m ² /s] |
| H | Hamaker constant [J] |
| h | specific enthalpy [J/kg] |
| i | imaginary unit $= \sqrt{-1}$ |
| J | evaporation mass flux [kg/(m ² ·s)] |
| L | length [m] |
| l | characteristic length scale [m] |
| M | total number of bubbles or plugs |
| m | mass [kg] |
| N | total number |
| Nu | Nusselt number |
| P | power [W] |
| p | pressure [Pa] |
| Q | heat amount [J] |
| q | heat flux [W/m ²] |
| R | gas constant [J/(kg·K)] |
| r | radius [m] |
| Re | liquid Reynolds number |
| S | surface area [m ²] |
| T | temperature [K] |
| t | time [s] |
| U | heat transfer coefficient [W/(m ² K)] |
| u | local fluid velocity [m/s] |

NOMENCLATURE

69

 V fluid velocity averaged over cross-section [m/s] w dewetting ridge width [m] x, y, z coordinates [m]*Abbreviations*

CFD computational fluid dynamics

CL contact line

EOS equation of state

PHP pulsating heat pipe

Greek symbols ΔT internal wall superheating, $T_w - T_{\text{sat}}$ [K] Δ difference δ thickness [m] γ vapor adiabatic index = c_{pv}/c_{vv} λ heat conductivity [W/(m·K)] μ liquid shear viscosity [Pa·s] ν liquid kinematic viscosity [m²/s] Ω vapor bubble volume [m³] ω angular frequency [s⁻¹] ϕ volume fraction of liquid in PHP ρ density [kg/m³] σ surface tension [N/m] τ shear stress at the solid wall [Pa] θ interfacial slope, contact angle φ film form factor, turn angle*Superscripts* s r or l i interfacial l left r right*Subscripts* i bubble or plug identifier number 0 initial a adiabatic section app apparent b branch c condenser cl contact line d dry area e evaporator f liquid film fb feedback PHP section (vertical in Fig. 1)

i internal
K Kelvin
l liquid
m meniscus
nucl nucleation
o outer tube wall
p PHP spatial period or at constant pressure
r reservoir
S Stokes
s slip
sat saturation
t total, tube
V Voinov
v vapor or at constant volume
w internal tube wall

References

- Akachi, H. (1993). Structure of micro-heat pipe, US Patent 5219020, URL https://www.lens.org/lens/patent/US_4921041_A.
- Aussillous, P. and Quéré, D. (2000). Quick deposition of a fluid on the wall of a tube, *Phys. Fluids* **12**, 10, pp. 2367 – 2371.
- Bajpai, A. K. and Khandekar, S. (2012). Thermal transport behavior of a liquid plug moving inside a dry capillary tube, *Heat Pipe Sci. Technol. Int. J.* **3**, 2-4, pp. 97 – 124.
- Baldassari, C. and Marengo, M. (2013). Flow boiling in microchannels and micro-gravity, *Prog. Energy Combust. Sci.* **39**, 1, pp. 1 – 36.
- Bretherton, F. P. (1961). The motion of long bubbles in tubes, *J. Fluid Mech.* **10**, pp. 166 – 188.
- Brochard-Wyart, F., Di Meglio, J.-M., Quere, D. and de Gennes, P.-G. (1991). Spreading of nonvolatile liquids in a continuum picture, *Langmuir* **7**, 2, pp. 335 – 338.
- Carey, V. P. (1992). *Liquid-Vapor Phase Change Phenomena* (Hemisphere, Washington D.C.).
- Chauris, N., Ayel, V., Bertin, Y. and Romestant, C. (2015). Evaporation of a liquid film deposited on a capillary heated tube: Experimental analysis by infrared thermography of its thermal footprint, *Int. J. Heat Mass Transfer* **86**, pp. 492 – 507.
- Cheng, P. and Ma, H. (2011). A mathematical model of an oscillating heat pipe, *Heat Transfer Eng.* **32**, 11-12, pp. 1037–1046.
- Daimaru, T., Nagai, H., Ando, M., Tanaka, K., Okamoto, A. and Sugita, H. (2017a). Comparison between numerical simulation and on-orbit experiment of oscillating heat pipes, *Int. J. Heat Mass Transfer* **109**, pp. 791 – 806.
- Daimaru, T., Yoshida, S. and Nagai, H. (2017b). Study on thermal cycle in oscillating heat pipes by numerical analysis, *Appl. Therm. Eng.* **113**, pp. 1219 – 1227.
- Darby, R. and Chhabra, R. P. (2017). *Chemical Engineering Fluid Mechanics*, 3rd edn. (CRC Press), ISBN 978-1-4987-2442-5.
- Das, S. P., Nikolayev, V. S., Lefèvre, F., Pottier, B., Khandekar, S. and Bonjour, J. (2010). Thermally induced two-phase oscillating flow inside a capillary tube, *Int. J. Heat Mass Transfer* **53**, 19-20, pp. 3905 – 3913.
- de Gennes, P.-G., Brochard-Wyart, F. and Quéré, D. (2004). *Capillarity and Wetting Phenomena: Drops, Bubbles, Pearls, Waves* (Springer, New York).
- de Gennes, P. G., Hua, X. and Levinson, P. (1990). Dynamics of wetting: local contact angles, *J. Fluid Mech.* **212**, pp. 55 – 63.
- Delon, G., Fermigier, M., Snoeijer, J. H. and Andreotti, B. (2008). Relaxation of a dewetting contact line. Part 2: Experiments, *J. Fluid Mech.* **604**, pp. 55 – 75.
- d'Entremont, B. P. and Thome, J. R. (2015a). A dynamic PHP model with tran-

- sient evaporating films, in *Proc. 9th Int. Conf. Boiling and Condensation Heat Transfer* (Boulder, USA).
- d'Entremont, B. P. and Thome, J. R. (2015b). A numerical study of pulsating heat pipe performance, in *Proc. InterPACKICNMM 2015*, p. V003T10A025.
- Dilawar, M. and Pattamatta, A. (2013). A parametric study of oscillatory two-phase flows in a single turn pulsating heat pipe using a non-isothermal vapor model, *Appl. Therm. Eng.* **51**, 1-2, pp. 1328 – 1338.
- Dobson, R. T. (2004). Theoretical and experimental modelling of an open oscillatory heat pipe including gravity, *Int. J. Therm. Sci.* **43**, 2, pp. 113 – 119.
- Eggers, J. (2005). Existence of receding and advancing contact lines, *Phys. Fluids* **17**, 8, p. 082106.
- Fischer, S., Gambaryan-Roisman, T. and Stephan, P. (2015). On the development of a thin evaporating liquid film at a receding liquid/vapour-interface, *Int. J. Heat Mass Transfer* **88**, pp. 346 – 356.
- Fourgeaud, L. (2016). *Analysis of the liquid film dynamics in a Pulsating Heat Pipe*, Ph.D. thesis, Université Grenoble-Alpes, URL <https://tel.archives-ouvertes.fr/tel-01409530>.
- Fourgeaud, L., Ercolani, E., Duplat, J., Gully, P. and Nikolayev, V. S. (2016). Evaporation-driven dewetting of a liquid film, *Phys. Rev. Fluids* **1**, 4, p. 041901.
- Fourgeaud, L., Nikolayev, V. S., Ercolani, E., Duplat, J. and Gully, P. (2017). In situ investigation of liquid films in pulsating heat pipe, *Appl. Therm. Eng.* **126**, pp. 1023 – 1028.
- Givler, R. C. and Martinez, M. J. (2009). Modeling of pulsating heat pipes, Tech. Rep. SAND2009-4520, Sandia Nat. Lab.
- Givler, R. C. and Martinez, M. J. (2013). Computational model of miniature pulsating heat pipes, Tech. Rep. SAND2012-4750, Sandia Nat. Lab.
- Gully, P., Bonnet, F., Nikolayev, V. S., Luchier, N. and Tran, T. Q. (2014). Evaluation of the vapor thermodynamic state in PHP, *Heat Pipe Science and Technology* **5**, 1-4, pp. 369 – 376.
- Gupta, R., Fletcher, D. and Haynes, B. (2010). Taylor flow in microchannels: A review of experimental and computational work, *J. Comput. Multiphase Flows* **2**, 1, pp. 1 – 31.
- Gürsel, G., Frijns, A. J. H., Homburg, F. G. A. and van Steenhoven, A. A. (2015). A mass-spring-damper model of a pulsating heat pipe with a non-uniform and asymmetric filling, *Appl. Therm. Eng.* **91**, pp. 80 – 90.
- Han, Y. and Shikazono, N. (2010). The effect of bubble acceleration on the liquid film thickness in micro tubes, *Int. J. Heat Fluid Flow* **31**, 4, pp. 630 – 639.
- Hao, T., Ma, X., Lan, Z., Li, N., Zhao, Y. and Ma, H. (2014). Effects of hydrophilic surface on heat transfer performance and oscillating motion for an oscillating heat pipe, *Int. J. Heat Mass Transfer* **72**, pp. 50 – 65.
- Hemida, H. N., Sabry, M. N., Abdel-Rahim, A. and Mansour, H. (2002). Theoretical analysis of heat transfer in laminar pulsating flow, *Int. J. Heat Mass Transfer*

REFERENCES

73

- 45, 8, pp. 1767 – 1780.
- Holley, B. and Faghri, A. (2005). Analysis of pulsating heat pipe with capillary wick and varying channel diameter, *Int. J. Heat Mass Transfer* **48**, 13, pp. 2635 – 2651.
- Idelchik, I. (2008). *Handbook of Hydraulic Resistance* (Jaico Publishing House), ISBN 9788179921180.
- Janeček, V., Andreotti, B., Pražák, D., Bárta, T. and Nikolayev, V. S. (2013). Moving contact line of a volatile fluid, *Phys. Rev. E* **88**, 6, p. 060404.
- Janeček, V. and Nikolayev, V. S. (2012). Contact line singularity at partial wetting during evaporation driven by substrate heating, *Europhys. Lett.* **100**, 1, p. 14003.
- Janeček, V. and Nikolayev, V. S. (2013). Apparent-contact-angle model at partial wetting and evaporation: impact of surface forces, *Phys. Rev. E* **87**, 1, p. 012404.
- Janeček, V. and Nikolayev, V. S. (2014). Triggering the boiling crisis: a study of the dry spot spreading mechanism, *Interfacial Phenom. Heat Transf.* **2**, 4, pp. 363 – 383.
- Khandekar, S., Panigrahi, P. K., Lefèvre, F. and Bonjour, J. (2010). Local hydrodynamics of flow in a pulsating heat pipe: a review, *Frontiers in Heat Pipes* **1**, 2, p. 023003.
- Khrustalev, D. and Faghri, A. (1997). Thick-film phenomenon in high-heat-flux evaporation from cylindrical pores, *J. Heat Transfer* **119**, 2, pp. 272 – 278.
- Kreutzer, M. T., Kapteijn, F., Moulijn, J. A., Kleijn, C. R. and Heiszwolf, J. J. (2005). Inertial and interfacial effects on pressure drop of Taylor flow in capillaries, *AIChE J.* **51**, 9, pp. 2428 – 2440.
- Kurzweg, U. H. and de Zhao, L. (1984). Heat transfer by high-frequency oscillations: A new hydrodynamic technique for achieving large effective thermal conductivities, *Phys. Fluids* **27**, 11, pp. 2624 – 2627.
- Lagubeau, G. (2006). *Propulsion par moteur pop-pop*, Master’s thesis, supervisor: D. Quéré, PMMH-ESPCI, Paris.
- Lauga, E., Brenner, M. P. and Stone, H. A. (2007). Microfluidics: The no-slip boundary condition, in C. Tropea, A. Yarin and J. Foss (eds.), *Springer Handbook of Experimental Fluid Dynamics*, chap. 19 (Springer, New York), pp. 1217 – 1240, <https://arxiv.org/pdf/cond-mat/0501557.pdf>.
- Li, P. and Yang, K. T. (2000). Mechanisms for the heat transfer enhancement in zero-mean oscillatory flows in short channels, *Int. J. Heat Mass Transfer* **43**, 19, pp. 3551 – 3566.
- Lips, S., Bensalem, A., Bertin, Y., Ayel, V., Romestant, C. and Bonjour, J. (2010). Experimental evidences of distinct heat transfer regimes in pulsating heat pipes (PHP), *Appl. Therm. Eng.* **30**, 8-9, pp. 900 – 907.
- Ma, H. (2015). *Oscillating Heat Pipes* (Springer, New York), ISBN 978-1-4939-2504-9.
- Magnini, M., Pulvirenti, B. and Thome, J. (2013a). Numerical investigation of hydrodynamics and heat transfer of elongated bubbles during flow boiling in a

- microchannel, *Int. J. Heat Mass Transfer* **59**, pp. 451 – 471.
- Magnini, M., Pulvirenti, B. and Thome, J. (2013b). Numerical investigation of the influence of leading and sequential bubbles on slug flow boiling within a microchannel, *Int. J. Therm. Sci.* **71**, pp. 36 – 52.
- Mameli, M., Marengo, M. and Zinna, S. (2012). Numerical model of a multi-turn closed loop pulsating heat pipe: Effects of the local pressure losses due to meanderings, *Int. J. Heat Mass Transfer* **55**, 4, pp. 1036 – 1047.
- Manzoni, M., Mameli, M., de Falco, C., Araneo, L., Filippeschi, S. and Marengo, M. (2016a). Advanced numerical method for a thermally induced slug flow: application to a capillary closed loop pulsating heat pipe, *Int. J. Numer. Methods Fluids* **82**, 7, pp. 375 – 397.
- Manzoni, M., Mameli, M., de Falco, C., Araneo, L., Filippeschi, S. and Marengo, M. (2016b). Non equilibrium lumped parameter model for pulsating heat pipes: validation in normal and hyper-gravity conditions, *Int. J. Heat Mass Transfer* **97**, pp. 473 – 485.
- Mehta, B. and Khandekar, S. (2014). Taylor bubble-train flows and heat transfer in the context of pulsating heat pipes, *Int. J. Heat Mass Transfer* **79**, pp. 279 – 290.
- Mehta, B. and Khandekar, S. (2015). Local experimental heat transfer of single-phase pulsating laminar flow in a square mini-channel, *Int. J. Therm. Sci.* **91**, pp. 157 – 166.
- Nagasaki, T., Sawada, Y., Hojo, S. and Ito, Y. (2011). Study on the mechanism of liquid column oscillation in a pulsating heat pipe, in *Proc. Nat. Heat Transfer Symp.* (Okayama, Japan), p. 87, in Japanese.
- Nekrashevych, I. and Nikolayev, V. S. (2017). Effect of tube heat conduction on the pulsating heat pipe start-up, *Appl. Therm. Eng.* **117**, pp. 24 – 29.
- Newton, I. (1687). *Philosophiae naturalis principia mathematica* (J. Societatis Regiae ac Typis J. Streater), URL https://play.google.com/store/books/details/Isaac_Newton_Philosophiae_naturalis_principia_math?id=WeZ09rjv-1kC, p.516.
- Nikolayev, V. S. (2010). Dynamics of the triple contact line on a nonisothermal heater at partial wetting, *Phys. Fluids* **22**, 8, p. 082105.
- Nikolayev, V. S. (2011a). Comment on “Flow and heat transfer of liquid plug and neighboring vapor slugs in a pulsating heat pipe” by Yuan, Qu, & Ma, *Int. J. Heat Mass Transfer* **54**, 9-10, pp. 2226 – 2227.
- Nikolayev, V. S. (2011b). A dynamic film model of the pulsating heat pipe, *J. Heat Transfer* **133**, 8, p. 081504.
- Nikolayev, V. S. (2013). Oscillatory instability of the gas-liquid meniscus in a capillary under the imposed temperature difference, *Int. J. Heat Mass Transfer* **64**, pp. 313 – 321.
- Nikolayev, V. S. (2016). Effect of tube heat conduction on the single branch pulsating heat pipe start-up, *Int. J. Heat Mass Transfer* **95**, pp. 477 – 487.

REFERENCES

75

- Nikolayev, V. S. and Beysens, D. A. (1999). Boiling crisis and non-equilibrium drying transition, *Europhys. Lett.* **47**, 3, pp. 345 – 351.
- Nikolayev, V. S. and Sundararaj, S. (2014). Oscillating menisci and liquid films at evaporation/condensation, *Heat Pipe Sci. Technol.* **5**, 1-4, pp. 59 – 67.
- Pai, P. F., Peng, H. and Ma, H. (2013). Thermomechanical finite-element analysis and dynamics characterization of three-plug oscillating heat pipes, *Int. J. Heat Mass Transfer* **64**, pp. 623 – 635.
- Pattamatta, A., Sielaff, A. and Stephan, P. (2015). A numerical study on the hydrodynamic and heat transfer characteristics of oscillating Taylor bubble in a capillary tube, *Appl. Therm. Eng.* **89**, pp. 628 – 639.
- Peng, H., Pai, P. F. and Ma, H. (2014). Nonlinear thermomechanical finite-element modeling, analysis and characterization of multi-turn oscillating heat pipes, *Int. J. Heat Mass Transfer* **69**, pp. 424 – 437.
- Potash, M. and Wayner, P. C. (1972). Evaporation from a two-dimensional extended meniscus, *Int. J. Heat Mass Transfer* **15**, 10, pp. 1851 – 1863.
- Pouryoussefi, S. M. and Zhang, Y. (2016a). Nonlinear analysis of chaotic flow in a three-dimensional closed-loop pulsating heat pipe, *J. Heat Transfer* **138**, 12, p. 122003.
- Pouryoussefi, S. M. and Zhang, Y. (2016b). Numerical investigation of chaotic flow in a 2D closed-loop pulsating heat pipe, *Appl. Therm. Eng.* **98**, pp. 617 – 627.
- Pouryoussefi, S. M. and Zhang, Y. (2017). Analysis of chaotic flow in a 2D multi-turn closed-loop pulsating heat pipe, *Appl. Therm. Eng.* **126**, pp. 1069 – 1076.
- Raj, R., Kunkelmann, C., Stephan, P., Plawsky, J. and Kim, J. (2012). Contact line behavior for a highly wetting fluid under superheated conditions, *Int. J. Heat Mass Transfer* **55**, 9-10, pp. 2664 – 2675.
- Rao, M., Lefèvre, F., Czujko, P.-C., Khandekar, S. and Bonjour, J. (2017). Numerical and experimental investigations of thermally induced oscillating flow inside a capillary tube, *Int. J. Therm. Sci.* **115**, pp. 29 – 42.
- Rao, M., Lefèvre, F., Khandekar, S. and Bonjour, J. (2013). Understanding transport mechanism of a self-sustained thermally driven oscillating two-phase system in a capillary tube, *Int. J. Heat Mass Transfer* **65**, pp. 451 – 459.
- Rao, M., Lefèvre, F., Khandekar, S. and Bonjour, J. (2015). Heat and mass transfer mechanisms of a self-sustained thermally driven oscillating liquid-vapour meniscus, *Int. J. Heat Mass Transfer* **86**, pp. 519 – 530.
- Recklin, V., Pattamatta, A. and Stephan, P. (2015). Experimental investigation on the thermo-hydrodynamics of oscillatory meniscus in a capillary tube using FC-72 as working fluid, *Int. J. Multiphase Flow* **75**, pp. 82 – 87.
- Sakulchangsatjatai, P., Chareonsawan, P., Waowaew, T., Terdtoon, P. and Murakami, M. (2008). Mathematical modeling of closed-end pulsating heat pipes operating with a bottom heat mode, *Heat Transfer Eng.* **29**, 3, pp. 239 – 254.
- Sakulchangsatjatai, P., Terdtoon, P., Wongratanaphisan, T., Kamonpet, P. and Murakami, M. (2004). Operation modeling of closed-end and closed-loop oscillating

- heat pipes at normal operating condition, *Appl. Therm. Eng.* **24**, 7, pp. 995 – 1008.
- Schlichting, H. (1968). *Boundary-Layer Theory* (McGraw-Hill, New York).
- Senjaya, R. and Inoue, T. (2013a). Bubble generation in oscillating heat pipe, *Appl. Therm. Eng.* **60**, 1-2, pp. 251 – 255.
- Senjaya, R. and Inoue, T. (2013b). Oscillating heat pipe simulation considering bubble generation. Part I: Presentation of the model and effects of a bubble generation, *Int. J. Heat Mass Transfer* **60**, pp. 816 – 824.
- Senjaya, R. and Inoue, T. (2013c). Oscillating heat pipe simulation considering bubble generation. Part II: Effects of fitting and design parameters, *Int. J. Heat Mass Transfer* **60**, pp. 825 – 835.
- Senjaya, R. and Inoue, T. (2014). Oscillating heat pipe simulation considering dryout phenomena, *Heat Mass Transfer* **50**, 10, pp. 1429 – 1441.
- Shafii, M. B., Faghri, A. and Zhang, Y. (2001). Thermal modeling of unlooped and looped pulsating heat pipes, *J. Heat Transfer* **123**, 6, pp. 1159 – 1172.
- Shao, W. and Zhang, Y. (2011). Effects of film evaporation and condensation on oscillatory flow and heat transfer in an oscillating heat pipe, *J. Heat Transfer* **133**, 4, p. 042901.
- Shikazono, N. and Han, Y. (2011). Liquid film thickness in micro-scale two-phase flow, in A. Ahsan (ed.), *Two Phase Flow, Phase Change and Numerical Modeling* (InTech), ISBN 978-953-307-584-6, pp. 341 – 364, URL <http://www.intechopen.com/books/two-phase-flow-phase-change-and-numericalmodeling/liquid-film-thickness-in-micro-scale-two-phase-flow>.
- Snoeijer, J. H. and Andreotti, B. (2013). Moving contact lines: Scales, regimes, and dynamical transitions, *Annu. Rev. Fluid Mech.* **45**, 1, pp. 269 – 292.
- Snoeijer, J. H., Delon, G., Fermigier, M. and Andreotti, B. (2006). Avoided critical behavior in dynamically forced wetting, *Phys. Rev. Lett.* **96**, 17, p. 174504.
- Snoeijer, J. H. and Eggers, J. (2010). Asymptotic analysis of the dewetting rim, *Phys. Rev. E* **82**, 5, p. 056314.
- Srinivasan, V., Marty-Jourjon, V., Khandekar, S., Lefèvre, F. and Bonjour, J. (2015). Evaporation of an isolated liquid plug moving inside a capillary tube, *Int. J. Heat Mass Transfer* **89**, pp. 176 – 185.
- Stephan, P. and Hammer, J. (1994). A new model for nucleate boiling heat transfer, *Heat Mass Transfer* **30**, 2, pp. 119 – 125.
- Talimi, V., Muzychka, Y. S. and Kocabiyik, S. (2012). A review on numerical studies of slug flow hydrodynamics and heat transfer in microtubes and microchannels, *Int. J. Multiphase Flow* **39**, pp. 88 – 104.
- Thome, J., Dupont, V. and Jacobi, A. (2004). Heat transfer model for evaporation in microchannels. Part I: presentation of the model, *Int. J. Heat Mass Transfer* **47**, 14-16, pp. 3375 – 3385.
- Wang, J., Ma, H. and Zhu, Q. (2015). Effects of the evaporator and condenser length on the performance of pulsating heat pipes, *Appl. Therm. Eng.* **91**, pp. 1018 – 1025.

REFERENCES

77

- Wörner, M. (2012). Numerical modeling of multiphase flows in microfluidics and micro process engineering: a review of methods and applications, *Microfluid. Nanofluid.* **12**, 6, pp. 841 – 886.
- Yin, D. and Ma, H. B. (2014). Analytical solution of heat transfer of oscillating flow at a triangular pressure waveform, *Int. J. Heat Mass Transfer* **70**, pp. 46 – 53.
- Yoon, A. and Kim, S. J. (2017). Characteristics of oscillating flow in a micro pulsating heat pipe: Fundamental-mode oscillation, *Int. J. Heat Mass Transfer* **109**, pp. 242 – 253.
- Yu, J.-C., Li, Z.-X. and Zhao, T. S. (2004). An analytical study of pulsating laminar heat convection in a circular tube with constant heat flux, *Int. J. Heat Mass Transfer* **47**, 24, pp. 5297 – 5301.
- Yuan, D., Qu, W. and Ma, T. (2010). Flow and heat transfer of liquid plug and neighboring vapor slugs in a pulsating heat pipe, *Int. J. Heat Mass Transfer* **53**, 7-8, pp. 1260 – 1268.
- Zhang, Y. and Faghri, A. (2002). Heat transfer in a pulsating heat pipe with open end, *Int. J. Heat Mass Transfer* **45**, 4, pp. 755 – 764.
- Zhang, Y. and Faghri, A. (2008). Advances and unsolved issues in pulsating heat pipes, *Heat Transfer Eng.* **29**, 1, pp. 20 – 44.
- Zhang, Y., Faghri, A. and Shafii, M. B. (2002). Analysis of liquid-vapor pulsating flow in a U-shaped miniature tube, *Int. J. Heat Mass Transfer* **45**, 12, pp. 2501 – 2508.
- Zhao, T. and Cheng, P. (1995). A numerical solution of laminar forced convection in a heated pipe subjected to a reciprocating flow, *Int. J. Heat Mass Transfer* **38**, 16, pp. 3011 – 3022.
- Zhao, T. S. and Cheng, P. (1996). Experimental studies on the onset of turbulence and frictional losses in an oscillatory turbulent pipe flow, *Int. J. Heat Fluid Flow* **17**, 4, pp. 356 – 362.